



# Quantitative T1 mapping using multi-slice multi-shot inversion recovery EPI

Rosa M. Sanchez Panchuelo<sup>a,b,\*</sup>, Olivier Mougín<sup>a</sup>, Robert Turner<sup>a,c</sup>, Susan T. Francis<sup>a,b</sup>

<sup>a</sup> Sir Peter Mansfield Imaging Centre, School of Physics and Astronomy, University of Nottingham, Nottingham, United Kingdom

<sup>b</sup> NIHR Nottingham Biomedical Research Centre, University of Nottingham, Nottingham, United Kingdom

<sup>c</sup> Max Planck Institute for Human Cognitive and Brain Sciences, Leipzig, Germany

## ARTICLE INFO

### Keywords:

Structural MRI  
Quantitative T1 mapping  
Multi-slice IR-EPI  
Fat suppression  
Neuroanatomy

## ABSTRACT

An efficient multi-slice inversion–recovery EPI (MS-IR-EPI) sequence for fast, high spatial resolution, quantitative T<sub>1</sub> mapping is presented, using a segmented simultaneous multi-slice acquisition, combined with slice order shifting across multiple acquisitions. The segmented acquisition minimises the effective TE and readout duration compared to a single-shot EPI scheme, reducing geometric distortions to provide high quality T<sub>1</sub> maps with a narrow point-spread function. The precision and repeatability of MS-IR-EPI T<sub>1</sub> measurements are assessed using both T<sub>1</sub>-calibrated and T<sub>2</sub>-calibrated ISMRM/NIST phantom spheres at 3 and 7 T and compared with single slice IR and MP2RAGE methods. Magnetization transfer (MT) effects of the spectrally-selective fat-suppression (FS) pulses required for *in vivo* imaging are shown to shorten the measured *in-vivo* T<sub>1</sub> values. We model the effect of these fat suppression pulses on T<sub>1</sub> measurements and show that the model can remove their MT contribution from the measured T<sub>1</sub>, thus providing accurate T<sub>1</sub> quantification. High spatial resolution T<sub>1</sub> maps of the human brain generated with MS-IR-EPI at 7 T are compared with those generated with the widely implemented MP2RAGE sequence. Our MS-IR-EPI sequence provides high SNR per unit time and sharper T<sub>1</sub> maps than MP2RAGE, demonstrating the potential for ultra-high resolution T<sub>1</sub> mapping and the improved discrimination of functionally relevant cortical areas in the human brain.

## 1. Introduction

Magnetic Resonance relaxometry techniques provide quantitative measures of the longitudinal (T<sub>1</sub>) relaxation time. T<sub>1</sub> relaxometry removes the confounding effects of sequence-related variations in the signal intensity in T<sub>1</sub>-weighted images – which are also weighted by proton density and T<sub>2</sub>\* – facilitating comparison across subjects, scanners and time to characterize the underlying physical composition of tissue, useful clinically in a wide range of applications (for a review, see Cheng et al. (2012)).

The T<sub>1</sub> relaxation time depends on the concentration of macromolecules such as proteins, phospholipids, polysaccharides and fat, and the degree of binding of water protons to the macro-molecules, with bound protons having a very short T<sub>1</sub>. Myelin has been shown to be the dominant source of T<sub>1</sub> contrast in the brain (Koenig et al., 1990; Callaghan et al., 2015; Rooney et al., 2007; Stüber et al., 2014; Leuze et al., 2017), causing T<sub>1</sub> shortening, although iron also contributes. Stüber et al. (2014) reported that iron makes an average contribution of 10% to T<sub>1</sub> in white matter and 36% to grey matter in fixed

cadaver human brain at 7 T, and Callaghan et al. (2015) showed that myelination is a better predictor of T<sub>1</sub> than iron content.

Myelin provides the neuronal basis of high processing speeds for high-level cognitive function (see Turner (2019) for a review of the role of myelin in the brain). Quantitative T<sub>1</sub>-maps have been used as a marker of myelination during brain development (Eminian et al., 2018; Kupeli et al., 2020) as well as to characterize white matter demyelination in clinical conditions (e.g. multiple sclerosis (Al-Radaideh et al., 2015)). The study of intracortical demyelination patterns is clinically relevant (Mougín et al., 2016; Beck et al., 2018) but still remains a challenge.

In systems neuroscience, quantitative T<sub>1</sub> maps can provide the basis for *in-vivo* cortical parcellation of distinct cortical areas (Turner, 2019). Ultra-high resolution structural MRI data can depict submillimeter-scale variations in image intensity across the cortical thickness, corresponding to variations in myelin density (e.g. Geyer et al., 2011; Glasser et al., 2016; Mougín et al., 2013; Sánchez-Panchuelo et al., 2012a; Sereno et al., 2013; Turner and Geyer, 2014); for a review, see (Trampel et al., 2019). This intracortical MRI contrast arises almost entirely from myeloarchitecture, rather than cytoarchitecture,

\* Corresponding author at: Sir Peter Mansfield Imaging Centre, University of Nottingham, Nottingham NG7 2RD, United Kingdom.

E-mail address: [rosa.panchuelo@nottingham.ac.uk](mailto:rosa.panchuelo@nottingham.ac.uk) (R.M. Sanchez Panchuelo).

<https://doi.org/10.1016/j.neuroimage.2021.117976>

Received 23 July 2020; Received in revised form 27 February 2021; Accepted 13 March 2021

Available online 26 March 2021

1053-8119/© 2021 The Author(s). Published by Elsevier Inc. This is an open access article under the CC BY license (<http://creativecommons.org/licenses/by/4.0/>)

although there may often be correspondence between the two (Dinse et al., 2015).  $T_1$  maps closely resemble myelin-stained histological sections (Geyer et al., 2011). Other studies have highlighted the correlation of observed cortical  $T_1$  contrast with known distributions of myelination (Glasser and van Essen, 2011; Lutti et al., 2014), paving the way for histological cortical parcellations *in-vivo*. Dinse et al. (2015) showed that a model based on archival cytoarchitectural data from cadaver brain could predict the cortical profile of *in-vivo* quantitative values of  $T_1$ , bridging the gap between the microanatomy revealed by classical histology and the macroanatomy visible in MRI. This work advocated a spatial resolution of 0.3 mm to reliably distinguish cortical areas based on intracortical features. However, this spatial resolution is beyond the limit of current  $T_1$  mapping methods *in-vivo* at ultra-high field (UHF, 7 T) and improvements in image acquisition are required to provide adequate ultra-high resolution quantitative  $T_1$  maps with a narrow point-spread function, maximal SNR per unit time, and low SAR.

A number of techniques have been proposed for  $T_1$  mapping. The inversion recovery (IR) method is considered the most accurate approach to measure  $T_1$ , acquiring multiple lines of k-space or images at a range of values of the time TI after a 180° inversion in order to sample the longitudinal magnetization recovery curve and derive an estimate of  $T_1$  by fitting the data to a mono-exponential function. However, the main disadvantage of this method is its temporal inefficiency. The gold standard sequence combines an IR with a spin-echo readout of a single line of k-space to limit the effect of  $B_1$  and  $B_0$  inhomogeneities, but the long acquisition time makes this impractical for human studies. Alternatively, the 2D approach can use an echo-planar imaging (EPI) readout to collect an image or series of multi-slice images after a given TI. While this significantly reduces the scan duration, spatial distortions can occur which are intrinsic to the use of single-shot EPI at high spatial resolution. Several methods have been proposed to improve the efficiency of  $T_1$  mapping including Look-Locker (LL) (Look and Locker, 1970) methods combined with FLASH (Deichmann et al., 1999) or EPI (Gowland and Mansfield, 1993) readouts which estimate  $T_1$  by collecting multiple read-outs to sample the longitudinal magnetization following a single  $T_1$ -recovery curve. However, the acquisition time remains long as the sequence must be repeated for multiple slices, although simultaneous multi-slice (SMS) strategies can now accelerate such acquisitions. A faster multi-slice inversion recovery variant was introduced (Ordidge et al., 1990) to allow the acquisition of quantitative  $T_1$  maps with whole brain coverage in 3 min. This sequence consists of a spatially non-selective adiabatic inversion pulse followed by the sequential acquisition of multiple slices with single-shot 2D EPI readouts, resulting in each slice being collected at a different inversion time. The slice ordering is then shifted in the next repeat of the data acquisition so that multiple points across the  $T_1$ -recovery curve are collected for each slice (Ordidge et al., 1990; Clare and Jezzard, 2001). If the total number of acquisitions repeated is less than the number of slices, then the computation of  $T_1$  maps requires the use of slice-specific inversion times, a method which has been shown to produce consistent  $T_1$  maps across a volume of 2D slices in a minimal acquisition time (Cohen and Polimeni, 2018; Lauzon et al., 2016; Polders et al., 2012; Renvall et al., 2016).

However,  $T_1$  maps collected using single shot EPI are prone to geometric distortions due to the low bandwidth in the phase-encode direction and  $B_0$ -field inhomogeneity. The MS-IR-EPI work presented in this manuscript aims to provide an alternative to the FLASH-based sequences for 'distortion-free'  $T_1$  mapping; however it should be noted that for some fMRI applications single-shot IR-EPI  $T_1$  maps are collected by design and intent to provide anatomical data with matched distortions to the fMRI data (Renvall et al., 2016). Such single-shot EPI  $T_1$  maps can be acquired with submillimeter (0.7 mm) spatial resolution over a small field of view to improve the accuracy of cortical depth definitions in fMRI data space (Huber et al., 2016; Kashyap et al., 2018). However, for the purpose of systematic cortical parcellation, a higher nominal spatial resolution (0.3 mm) is required over larger brain volumes. For this to be

achieved the readout window and effective echo time of single-shot EPI would become prohibitively long, with consequent unacceptable image blurring.

Currently, the most popular method of  $T_1$  mapping used at UHF is the 'Magnetization-Prepared 2 Rapid Gradient Echoes' (MP2RAGE) sequence (Van de Moortele et al., 2009; Marques et al., 2010). This combines two Gradient-Recalled Echo (GRE) 3D volumes acquired at two different inversion times (the first predominantly  $T_1$ -weighted and the second PD-weighted) within a single repetition time to calculate a quantitative  $T_1$  map based on the  $T_1$ -weighted combination image, which is free from bias-field effects, and the use of a look-up table. A non-selective adiabatic inversion pulse is used to minimize sensitivity to the inhomogeneity of transmit  $B_1$  field ( $B_1^+$ ) at 7 T (Hurley et al., 2010). Deviation of the nominal excitation flip angles in the GRE trains caused by inhomogeneity in  $B_1^+$  can lead to bias in the  $T_1$  estimation, particularly when a large number of low flip angle excitation pulses are used (Marques and Gruetter, 2013) as required for submillimeter spatial resolution. The further application of a  $B_1$ -mapping sequence can provide estimates of the effective excitation flip angle and thus improve the accuracy of MP2RAGE based  $T_1$  mapping (Marques and Gruetter, 2013; Haast et al., 2018), enabling measurement of cortical thickness using quantitative  $T_1$  maps (Haast et al., 2018). However, for ultra-high spatial resolution measures the resulting 3D GRE train is long, of the order of tissue  $T_1$ , resulting in a relatively broad point spread function (PSF) and long total scan duration for sufficient SNR. When MP2RAGE is used at nominal spatial resolution of the order of 0.3 mm to depict intracortical details, these invariably appear blurred, even on trained subjects when no apparent motion is detected or when motion is prospectively corrected (Federau and Gallichan, 2016).

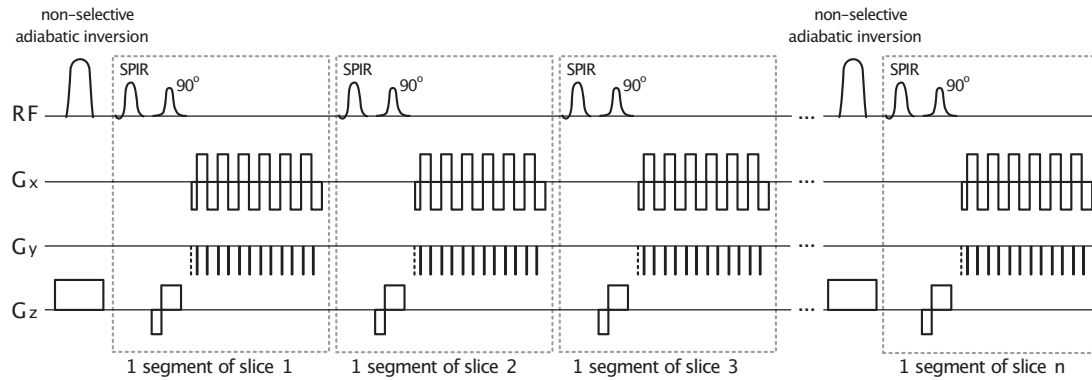
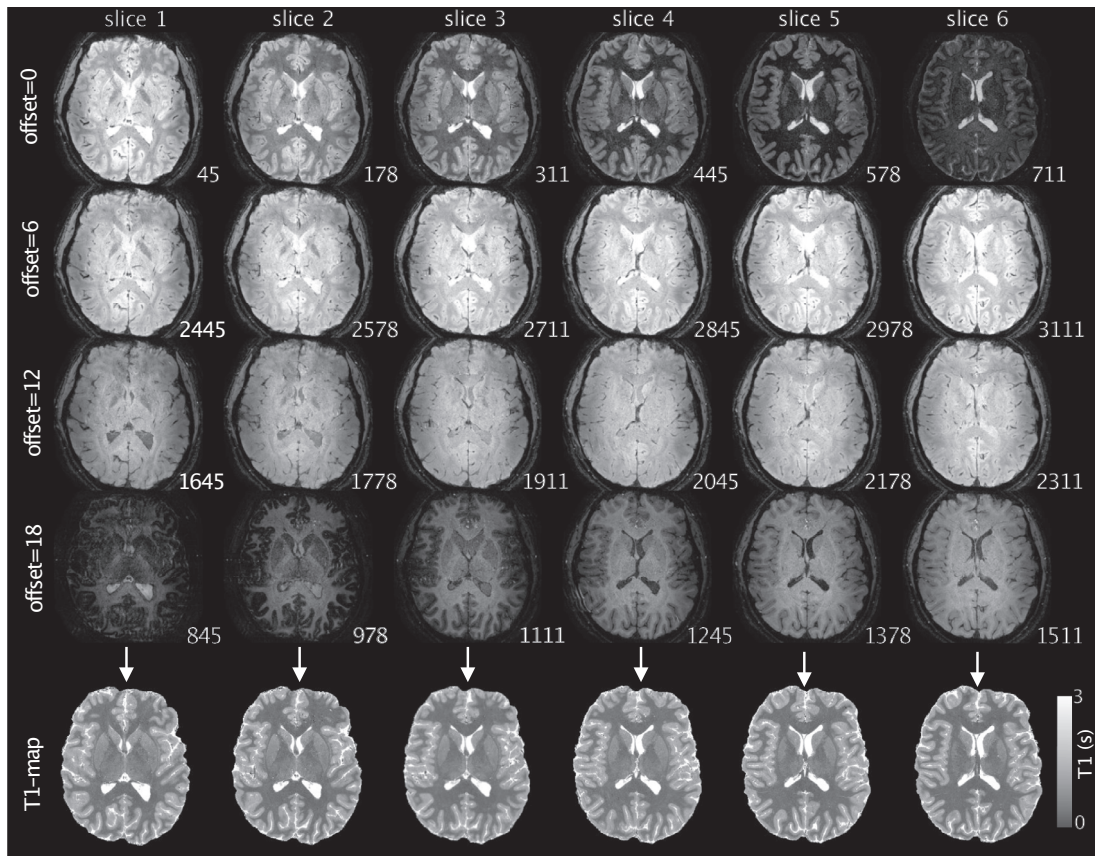
In this present study, we aimed to implement a fast multi-slice multi-shot inversion-recovery 2D-EPI  $T_1$  mapping method which fills all the recovery time between each inversion pulse with acquisition of k-space segments of each slice, keeping the effective TE and acquisition time to a minimum to reduce geometric distortions, and resulting in a narrow point-spread function. It has been shown that the value of  $T_1$  in the brain is largely determined by magnetization transfer (MT) between the free water proton pool and the macromolecule-bonded proton pool (Koenig et al., 1990; Turner et al., 2008; Shin et al., 2009). The feature of short-TE EPI sequences which contributes most to magnetization transfer effects is the fat suppression pulse that normally accompanies each spin excitation pulse. To explore the possibility of accurate  $T_1$  quantification, we assessed the impact of MT effects due to multi-slice acquisitions and the spectrally selective fat suppression pulses on  $T_1$  quantification that we employed. We propose a model to remove the MT contribution from the derived  $T_1$ . The approach is combined with simultaneous multi-slice (SMS) acquisition techniques to improve spatial coverage.

We hypothesise that: (a) MS-IR-EPI produces  $T_1$  maps at 7 T with accuracy and repeatability comparable to MP2RAGE and multi-shot single slice IR-EPI, but in a faster time; (b) MS-IR-EPI provides  $T_1$  maps with higher SNR per unit time than MP2RAGE; (c) the MT effects due to spectrally selective fat suppression pulses in MS-IR-EPI can be effectively removed for accurate  $T_1$  quantification; (d) MS-IR-EPI  $T_1$  maps yield sharper images than MP2RAGE with the same nominal spatial resolution, and can be used for intracortical mapping.

## 2. Methods

### 2.1. Multi-shot inversion-recovery 2D echo-planar imaging (MS-IR-EPI) sequence

Fig. 1 illustrates the multi-shot multi-slice inversion-recovery EPI (MS-IR-EPI) sequence that was implemented. A non-selective adiabatic inversion is used for homogeneous inversion across the imaging volume. The time between successive inversions is filled with slice-selective 90° excitation pulses, each followed by a segmented gradient echo (GE)

**(A) MS-IR-EPI sequence diagram****(B) Slice shifting method**

**Fig. 1.** (A) 2D multi-shot inversion recovery EPI sequence diagram: A non-selective adiabatic inversion pulse of slab thickness 200 mm is rapidly followed by a series of multi-slice-selective 90° excitation pulses (spectrally selective SPIR pulses applied for fat suppression). A segment of k-space is acquired after each excitation in order to keep the acquisition window short, to minimize image distortion and dropout and ensure a well-defined inversion time and a narrow point-spread function. In order to generate T<sub>1</sub> maps, multiple acquisitions are performed with varying slice acquisition order by adding a slice offset to the ascending slice order. (B) Example sub-set of slices (6 of 24) acquired using 2D MS-IR-EPI (0.5 × 0.5 × 1.5mm<sup>3</sup>, TR=3.2 s). Data is shown for four slice offsets of [0,6,12,18] (each row). The different contrast across the slices reflects the different acquired T<sub>1</sub>s (ms); Note that for each slice the 4 T<sub>1</sub>s are equally spaced at 800 ms intervals across offsets. The corresponding T<sub>1</sub> map generated for each slice is shown in the bottom row.

EPI acquisition window. The segmented acquisition, whose duration is a small fraction of T<sub>1</sub>, is used to provide a well-defined inversion time for each segment and consequently a narrow point-spread function, while multiple shots are required to sample the entire k-space plane. This sequence can be used with in-plane acceleration and SMS excitation pulses to achieve whole brain coverage even more quickly (Dougherty et al., 2014; Grinstead et al., 2014). Multiple volume acquisitions (N<sub>acq</sub>) are collected in which the slice order is shifted by a constant offset number, resulting in a set of equally spaced distinct inversion times for each seg-

ment (shown in Fig. 1 for 800 ms temporal slice offset). The slice acquisitions are equally distributed within the TR period after the minimum inversion time (~44.5 ms), and there is no dead time during the recovery of longitudinal magnetization. Note, in contrast to single-shot IR-EPI, the recovery time remains constant across all segments of the multi-shot acquisition, except for when transitioning between slice offset number. The collection of complex data allows the phase data to be employed to correct the polarity in the slice-by-slice computation of T<sub>1</sub> maps using the modulus corrected data, resulting in a mono-exponential T<sub>1</sub>-

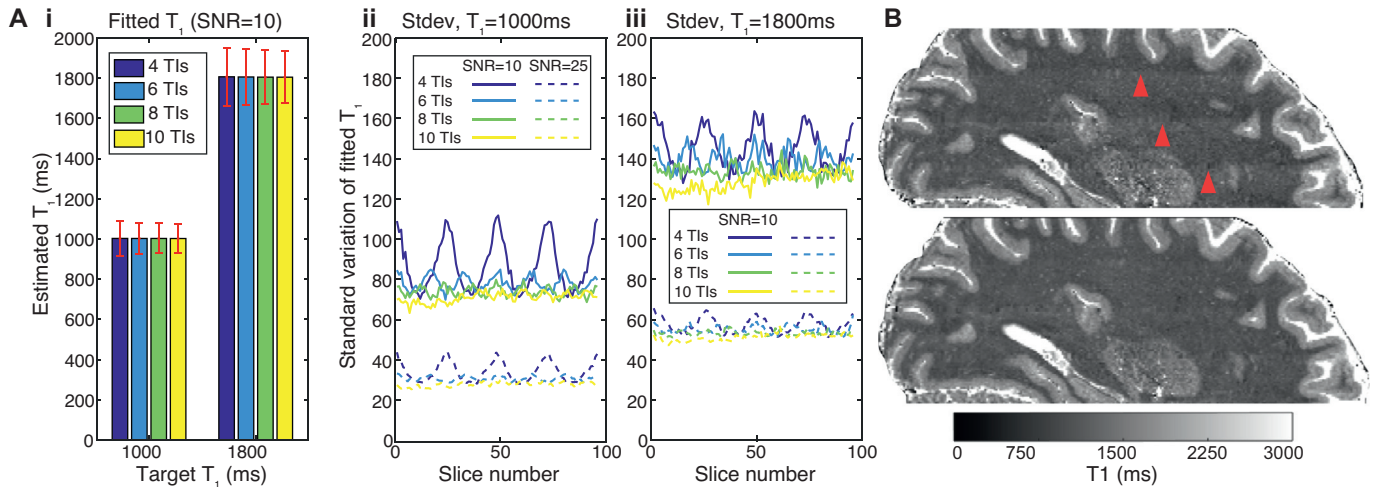


**Fig. 2.** (A) Monte Carlo simulations of the multi-shot inversion recovery EPI sequence showing the effect of number of acquisition/TIs (4,6,8,10) on fitted  $T_1$  parameters. Simulations were performed for a target  $T_1$  of 1 s (~WM) and 1.8 s (~GM), SNR=10 and 25, TR=5 s and 96 slices. Gaussian noise was added to the simulated complex data (with 1024 repeats) which was fit after sign correction, as for the experimental data, to obtain mean and standard deviation of fitted  $T_1$  values. Fig. 2Ai). The fitted  $T_1$  (mean across slices) remains constant but the standard deviation (error bars) decreases with increasing number of TIs (shown for SNR=10). Fig. 2A ii) plots the standard deviation of the fitted  $T_1$ -values across each of 96 slices for SNR=10 (solid lines) and SNR=25 (dash lines) showing that for WM there is a variation of the fitted  $T_1$  value across slices when using 4 and 6 TIs whereas in Fig. 2A iii) for GM the variation is only obvious when using only 4 TIs. (B) Sagittal reconstructions of the axial  $T_1$ -maps derived using 4 (top) and 8 (bottom) equally spaced TIs. Note the  $T_1$  maps derived from 4 TI data show banding within the WM tissue (red arrowheads) not evident in the  $T_1$  map derived from 8 TIs, in agreement with simulations. (For interpretation of the references to colour in this figure legend, the reader is referred to the web version of this article.)

recovery curve:  $S(TI) = S_0[1 - 2\exp(-TI/T_1) + \exp(-TR/T_1)]$ , which can easily be fit using a least squares regression. The  $S_0$  image provided by the fit represents the proton density weighted by the effective transverse relaxation time  $T_2^*$ .

## 2.2. Monte Carlo simulations to optimize sampling for the MS-IR-EPI sequence

Since the MS-IR-EPI method computes a  $T_1$  map from the different inversion times experienced by each slice, care must be taken to ensure that the sampling of the inversion times across all slices provides consistent  $T_1$  values. The minimum TI each slice experiences has a key impact on the measured  $T_1$ , especially for lower  $T_1$  values, and this can lead to banding artefacts observed in the slice direction when an insufficient number of acquisitions are performed (and hence the minimum TI values sampled). To test the robustness of the  $T_1$  fitting to the range of acquisition strategy and noise level, a Monte Carlo (MC) simulation of the entire fitting algorithm (including the phase correction) was implemented. Each MC run included 1024 samples with gaussian distributed noise added to the complex signal, at SNR levels of 10 and 25, and target TIs of 1000 and 1800 ms. The MC simulation was used to determine the minimum number of acquisitions ( $N_{\text{acq}}$  and thus inversion times) needed to obtain homogenous  $T_1$  maps across the multiple slices of the data set (Fig. 2 and Supplementary Material Figure 1). We assessed  $N_{\text{acq}}$  for whole brain 0.7 mm isotropic resolution at 7 T (for a TR of 5 and 3.2 s with SMS factors of 2 and 3 respectively), and whole brain 1 mm isotropic resolution at 3 T (for a TR of 4.5 s with SMS factor 2) (See Table 1 and ‘ $T_1$  mapping data acquisition’ section).

## 2.3. $T_1$ mapping acquisitions

Scanning was performed on a 7 T Philips Achieva system and 3 T Philips Ingenia system, both equipped with a 32-channel receive array NOVA coil. The 7 T whole head MS-IR-EPI protocol comprised a field of view (FOV) of 192(AP) x 164(RL) mm<sup>2</sup> with 0.7 mm isotropic resolution using protocols MS1 and MS2 outlined in Table 1 with SMS factors of 2 and 3 respectively.

At 3 T, 1 mm isotropic MS-IR-EPI data with whole brain coverage (192 × 192 × 192 mm<sup>3</sup>) were acquired using protocol MS5 parameters with a SMS factor of 2 (Table 1). All MS-IR-EPI protocols acquired contiguous slices in ascending order with phase encoding in the RL direction. The maximum EPI factor used was 15 (see Table 1) to provide  $T_1$  maps with minimal distortion (see Fig. 5, Sanchez Panchuelo et al., 2018). This factor was lowered in some protocols in order to increase the number of slices required to achieve whole brain coverage (for the specific TR and SMS factor). For comparison to the MS-IR-EPI method, MP2RAGE data with 0.7 mm and 1 mm isotropic resolution were acquired at 7 and 3 T respectively (see Table 1: MP1 (parameters based on Dinse et al. (2015)) and MP3 protocols). A TR-FOCI pulse was used for adiabatic inversion at 7 T (see Hurley et al. (2010) for details of the TR-FOCI pulse). MP2RAGE acquisitions were followed by a DREAM B<sub>1</sub>-map acquisition (4.5 mm isotropic resolution, FOV=288(AP)x252(RL)x198(FH) mm<sup>3</sup>, SENSE factor=2 (RL), FA=8°, TE=1 ms, TR=2.3 ms, Turbo-Field-Echo factor=890, acquisition bandwidth=5351 Hz, 2.2 s acquisition time) to allow computation of the effective excitation flip angles in the MP2RAGE trains for improved accuracy of the  $T_1$  fit (Marques and Gruetter, 2013). An MP2RAGE image ( $S_{\text{MP2RAGE}}$ ) was formed based on the combination of the two complex images,  $S_{\text{MP2RAGE}} = (S_{\text{TI1}} \times S_{\text{TI2}}^*) / (S_{\text{TI1}}^2 + S_{\text{TI2}}^2)$ , where the asterisk indicates the complex conjugate. A look-up table was used in order to estimate  $T_1$  maps from the  $S_{\text{MP2RAGE}}$  values (Marques et al., 2010).

## 2.4. Validation of MS-IREPI using $T_1$ -calibrated and $T_2$ -calibrated ISMRM/NIST spheres

The precision and repeatability of the optimized MS-IR-EPI sequence were assessed using the International Society for Magnetic Resonance in Medicine (ISMRM)/National Institute of Standards and Technology (NIST) fiducial  $T_1$  and  $T_2$  spheres (Kenan et al., 2016). The NIST  $T_1$  spheres contain specific concentrations of NiCl<sub>2</sub> solution to provide a known range of  $T_1$  values at 3T. The first ten ( $T_{1\_1}$  to  $T_{1\_10}$ ) calibrated  $T_1$ -spheres, with  $T_1$  values ranging from 1998 ms ( $T_{1\_1}$ ) to 89 ms ( $T_{1\_10}$ ) at 3 T (Kenan et al., 2016) were used. The  $T_2$  spheres are doped with

**Table 1**  
Parameters used in MS-IR-EPI and MP2RAGE protocols at 7 T and 3 T. For MS-IR-EPI, BW provided in frequency (FE) and phase (PE) encoding direction, SAR provided for SMS option (if used). The SAR for MS1 in the absence of fat suppression was <1.1 kg/W.

MS-IR-EPI													
Protocol	B <sub>0</sub>	Voxel (mm <sup>3</sup> )	TR (s)	EPI factor	BW <sub>FE/PE</sub> (Hz)	TE (ms)	SENSE factor	SMS factor	SPR FA(°)	SAR (W/kg)	Slice offsets	Acquisition time	
MS1	7T	0.7 <sup>3</sup>	5	15	856/61	16	2	1&2	70	<1.6	0,12,24,36,48,60,72,84	4 min 50s	
MS2	7T	0.7 <sup>3</sup>	3.2	13	884/74	16	1.6	1&3	0	<1.3	0,13, 26, 39, 52	2 min 56s	
MS3	7T	0.5 <sup>3</sup>	3.8	7	625/104	14	1.6	3	90	<2.8	0, 8, 16, 24, 32, 40, 48, 56, 64, 72	18 min 22s	
MS4	7T	0.35 <sup>2</sup> ×0.7	3.2	13	492/41	20	2	1	60	<1.1	[0, 7, 14, 21, 28]×3	11 min 8s	
MS5	3T	1 <sup>3</sup>	4.5	11	951/95	11	3	2	0	<0.1	0,12,24,36,48,60,72,84	3 min 54s	
MP2RAGE													
Protocol	B <sub>0</sub>	Voxel (mm <sup>3</sup> )	TR <sub>shot</sub> (s)	T <sub>1</sub> (ms)	T <sub>1,2</sub> (ms)	TE/TR (ms)	TFE factor	FA <sub>1</sub> /FA <sub>2</sub>	SENSE factor	TFE <sub>req</sub> (ms)	BW (Hz)	SAR (W/kg)	Acquisition time
MP1	7T	0.7 <sup>3</sup>	5	900	2757	2.5/5.5	224	5/3 °	3	1230	337	<0.9	8 min 55s
MP2	7T	0.35 <sup>2</sup> ×0.7	4	900	2375	9/18	70	5/2 °	2	1277	67.2	<1.1	12 min 8s
MP3	3T	1 <sup>3</sup>	5.5	700	2500	3/7.1	118	5/3 °	3 × 1.5	838	228	<0.1	7 min 10s

specific concentrations of MnCl<sub>2</sub> and also provide well characterized T<sub>1</sub> values at 3 T, with the first ten (T<sub>2\_1</sub> to T<sub>2\_10</sub>) T<sub>2</sub>-spheres ranging from 3025 ms (T<sub>2\_1</sub>) to 293 ms (T<sub>2\_10</sub>). Note that the reference T<sub>1</sub> values provided by the manufacturer for spheres T<sub>2\_1</sub> and T<sub>2\_5</sub> reflect measurements known to be deviant from the MnCl<sub>2</sub> nominal solutions due to a problem at the time of the manufacturing process of our phantom. Due to the reduced size of the 7 T NOVA head coil compared to a 3 T head coil, home-built casings were manufactured to fit each plate of T<sub>1</sub>-spheres and T<sub>2</sub>-spheres within a separate 160 mm diameter spherical phantom that would fit within the 7 T NOVA head coil.

Due to the poor accuracy of measured B<sub>1</sub> in the short T<sub>1\_7</sub> to T<sub>1\_14</sub> spheres (as reported in Kato et al., 2019) (see Supplementary Material, Fig. 3), only spheres T<sub>1\_1</sub> to T<sub>1\_6</sub>, with T<sub>1</sub> values within the clinically relevant dynamic range (300 to 2000 ms) of the brain tissues, were considered for analysis, in line with recent studies at 3 T (Hagiwara et al., 2019; Kato et al., 2019).

To compare the accuracy of the MS-IR-EPI method with other T<sub>1</sub> mapping methods, the T<sub>1</sub> and T<sub>2</sub> phantoms were scanned at 3T using: (i) a gold-standard IR-TSE sequence using the ISMRM/NIST recommended parameters: a single 6 mm slice with 0.98 × 0.98 mm<sup>2</sup> in-plane resolution, TR/TE= 4.5 s/7 ms repeated for a range of inversion times TIs (ms) = [35, 75, 100, 125, 150, 250, 1000, 1500, 2000, 3000], 35 min acquisition, (ii) MS-IR-EPI, and (iii) an MP2RAGE acquired at 1 mm isotropic resolution (parameters in Table 1). All measurements were repeated at a second and third session for the T<sub>1</sub>-spheres phantom (6 and 9 months apart) and a second scan session (1 week apart) for the T<sub>2</sub>-spheres phantom. The temperature of each phantom (in the solution surrounding the spheres) was measured across the scan sessions. The mean T<sub>1</sub> values across scan sessions was computed using each of the T<sub>1</sub> mapping methods and compared to the NIST reference T<sub>1</sub> values.

The phantoms were also scanned at 7 T to acquire 0.7 mm isotropic data using: (i) a single slice multi-shot IR-EPI acquisition at a range of TIs (ms) = [35, 75, 100, 150, 250, 500, 1000, 2000, 3000] with other acquisition parameters matched to the MS-IR-EPI, (ii) MS-IR-EPI (TR 5 s) and (iii) MP2RAGE sequences (parameters described in Table 1). All measurements were repeated multiple times for test and re-test reproducibility assessment. In total, 6 measurements were collected (second repeat after 40 days, and repeats 3–6 at 9 months over a 10-day period) for the T<sub>1</sub>-spheres phantom and 4 measurements (repeated with 2–3 day intervals) were collected for the T<sub>2</sub>-spheres phantom, again temperature was measured in the phantoms after each scan session. Repeatability was characterized by the coefficient of variation (CoV), defined as the ratio between the standard deviation and the mean T<sub>1</sub> values across all repeat measurements (Kato et al., 2019). T<sub>1</sub> values obtained with MS-IR-EPI and MP2RAGE were compared to those obtained with the reference single slice IR-EPI method.

Further scan sessions were performed in which two measurements of sequences (ii) and (iii) were collected for the NIST T<sub>1</sub>-spheres phantom in order to assess SNR per unit time of the generated T<sub>1</sub> maps. In addition, two repeats were collected of the MS-IR-EPI sequence at a shorter TR of 3.2 s (EPI=13, TE=13 ms, 4TIs) using SMS factor 1 (92 slices) and SMS factor 2 (184 slices). To estimate image SNR, T<sub>1</sub> maps generated from each individual run were subtracted to provide a ‘noise’ map. For each region of interest (ROI), SNR was estimated as the mean across voxels (in both T<sub>1</sub> maps) divided by the standard deviation of the noise map. For each sequence, SNR per unit time was computed by dividing the image SNR by the total acquisition time (in minutes).

### 2.5. In-vivo experiments

Five subjects (2 female, age: 32±6years (mean±SEM)) were recruited to the study. Experimental procedures for all studies were approved by the University of Nottingham Medical School’s Ethics Committee. All subjects gave written informed consent. None of the subjects had a history of neurological disorders.

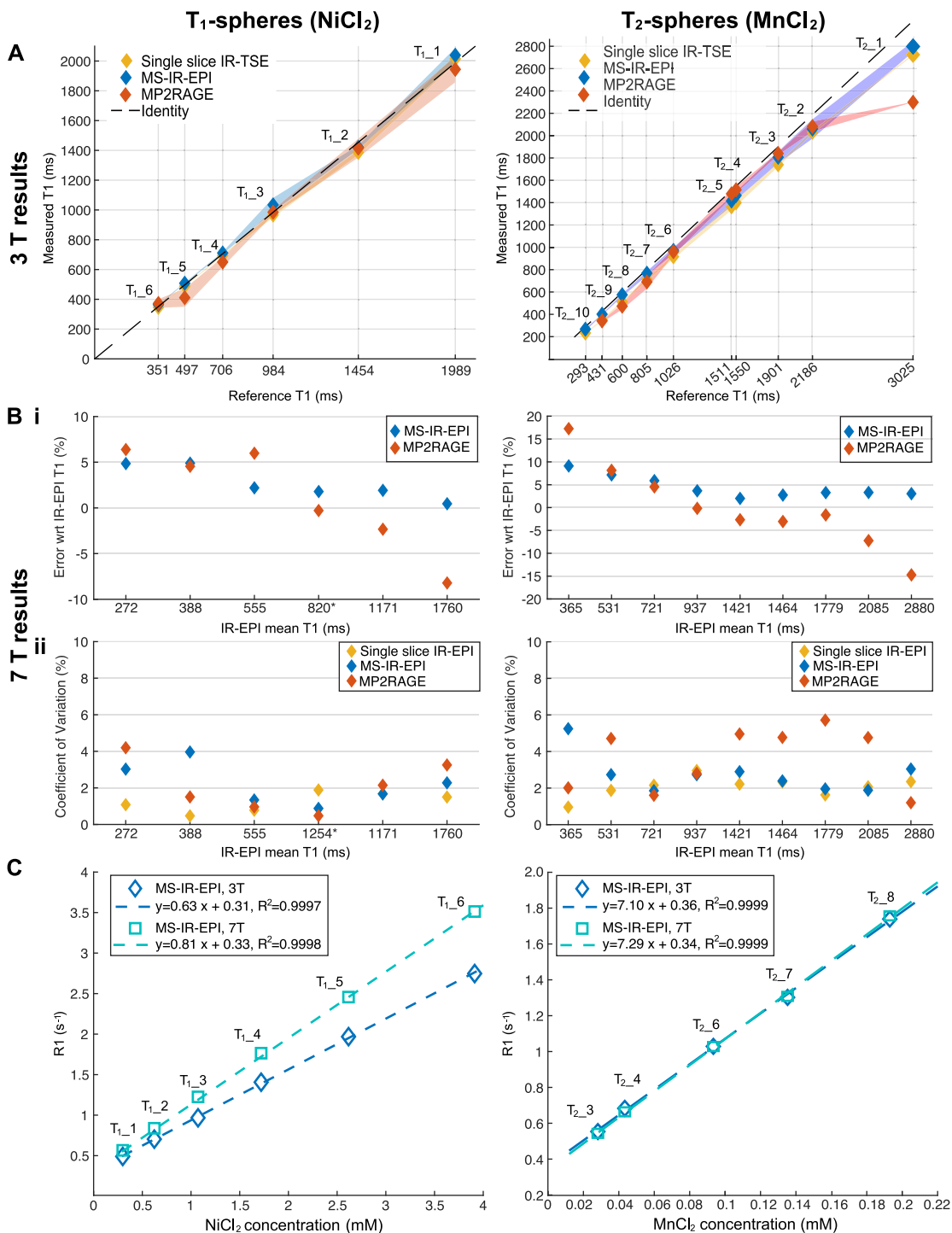


**Fig. 3.** Phantom results using the ISMRM/NIST system T<sub>1</sub> (left column) and T<sub>2</sub> (right column) spheres. (A) Scatter plots showing linearity of measured T<sub>1</sub> (ms) for the single slice IR-TSE, MS-IR-EPI and MP2RAGE plots against reference T<sub>1</sub> values provided by NIST for 3 T. The error surface shows the standard deviation across 3 (T<sub>1</sub>-spheres) and 2 (T<sub>2</sub>-spheres) measurements, except for T<sub>1\_3</sub> sphere (standard deviation across voxels from a single session). The dashed line represent identity. (B) (i) The relative deviation of MS-IR-EPI and MP2RAGE T<sub>1</sub> measurements at 7 T with respect to the single slice IR-EPI T<sub>1</sub> measurements. T<sub>1</sub>-value measures averaged across 6 (T<sub>1</sub>-spheres) and 4 (T<sub>2</sub> spheres) measurements. \*Note that for T<sub>1\_3</sub> sphere T<sub>1</sub> values are average across voxels within a single measurement (see Supplementary Material). (ii) Coefficient of variation (CoV) showing the repeatability of T<sub>1</sub> measures by the different methods at 7 T. \*Note that the CoV for T<sub>1\_3</sub> sphere was computed over the last 4 measurements. (D) Plots of R<sub>1</sub> (s<sup>-1</sup>) values obtained with the MS-IR-EPI at 3 and 7 T versus the NiCl<sub>2</sub> (left) and MnCl<sub>2</sub> (right) nominal concentration (mM<sup>-1</sup>). Dashed lines represent linear regression fit. (For interpretation of the references to colour in this figure legend, the reader is referred to the web version of this article.)

**Table 2**

Comparison of (A)  $T_1$  values (in ms, given by histogram peak), (B) histogram peak height and (C) full width at half maximum, for data acquired with no fat suppression (reference) and with fat suppression before and after correction using a constant  $b/a$  value (global correction) and  $(b/a)$  map (voxelwise correction). Results shown for data acquired with  $70^\circ$  flip angle SPIR pulse. Global correction based on  $b/a$  data computed from datasets of 5 and 2 FAs.

(A) $T_1$ (ms)		Subject 1	Subject 2	Subject 3	Mean $\pm$ std
FS= $0^\circ$ (reference)	GM	1694	1697	1706	1699 $\pm$ 6
	WM	1135	1063	1156	1118 $\pm$ 49
FS= $70^\circ$ (no correction)	GM	1372	1438	1454	1421 $\pm$ 43
	WM	910	878	933	907 $\pm$ 28
FS= $70^\circ$ corrected with $(b/a)$ map	GM	1846	1831	1786	1814 $\pm$ 31
	WM	1285	1177	1253	1238 $\pm$ 5
FS= $70^\circ$ corrected with global $(b/a)$ -5pts	GM	1785	1783	1814	1794 $\pm$ 17
	WM	1194	1102	1175	1157 $\pm$ 49
FS= $70^\circ$ corrected with global $(b/a)$ -2pts	GM	1783	1751	1783	1772 $\pm$ 18
	WM	1182	1090	1164	1145 $\pm$ 49
(B) Histogram peak height with respect to reference (FS= $0^\circ$ )					
FS= $70^\circ$ (no correction)	GM	81%	81%	83%	82 $\pm$ 1%
	WM	76%	65%	66%	69 $\pm$ 6%
FS= $70^\circ$ corrected with $(b/a)$ map	GM	96%	88%	107%	97 $\pm$ 10%
	WM	103%	78%	87%	89 $\pm$ 13%
FS= $70^\circ$ corrected with global $(b/a)$ -5pts	GM	114%	107%	111%	111 $\pm$ 4%
	WM	110%	85%	88%	94 $\pm$ 14%
FS= $70^\circ$ corrected with global $(b/a)$ -2pts	GM	114%	105%	109%	109 $\pm$ 4%
	WM	108%	85%	87%	93 $\pm$ 13%
(C) Histogram FWHM with respect to reference (FS= $0^\circ$ )					
FS= $70^\circ$ (no correction)	GM	137%	139%	149%	142 $\pm$ 7%
	WM	137%	155%	173%	155 $\pm$ 18%
FS= $70^\circ$ corrected with $(b/a)$ map	GM	106%	117%	117%	113 $\pm$ 6%
	WM	100%	133%	129%	121 $\pm$ 18%
FS= $70^\circ$ corrected with global $(b/a)$ -5pts	GM	93%	108%	108%	103 $\pm$ 8%
	WM	93%	122%	134%	116 $\pm$ 21%
FS= $70^\circ$ corrected with global $(b/a)$ -2pts	GM	93%	99%	116%	103 $\pm$ 12%
	WM	93%	122%	134%	116 $\pm$ 21%

### 2.5.1. Effect of TR, SMS factor and number of slices on MS-IR-EPI $T_1$ -mapping at 7 T

To assess the effect on the measured  $T_1$  of shortening the TR, a subject was scanned at 7 T using MS-IR-EPI protocols with TR=5 s and TR=3.2 s (MS1 and MS2 respectively in Table 1). Data were acquired using SMS=1 (96 slices) and SMS=2 (192 slices) with protocol MS1 and using SMS=1 (65 slices) and SMS=3 (195 slices) with protocol MS2, to determine whether the different RF excitation pulses used in the SMS acquisition change the measured  $T_1$  relative to SMS=1. In a second scan session, to assess whether  $T_1$  measurements are shortened due to residual MT effects from RF pulses selecting neighbouring slices, acquisitions of the MS-IR-EPI TR=3.2 s (5 TIs) protocol were repeated with varying number of slices, ns=[65, 35, 15, 5]. For this, the coverage in the slice direction across the different acquisitions was maintained by varying the slice gap: sg=[0, 0.7, 2.8, 10.5] mm for ns=[65,35,15,5] respectively. A single slice IR-EPI acquisition (with parameters matched to the MS-IR-EPI acquisition) was also collected with TI values=[320, 900, 1470, 2050, 2625] ms for comparison with the central slice of the MS-IR-EPI acquisitions. All data sets were acquired without using spectrally selective fat suppression pulses.

### 2.5.2. Characterizing the effect of fat suppression pulses on the measured $T_1$

Experiments were performed in three subjects using the 0.7 mm isotropic resolution MS-IR-EPI MS1 protocol (Table 1) to measure the longitudinal relaxation rate,  $R_1(r)$ , for a range of nominal flip angles (FA)=[ $0^\circ$ ,  $30^\circ$ ,  $40^\circ$ ,  $50^\circ$ ,  $60^\circ$ ,  $70^\circ$ ] of the SPIR (spectral pre-saturation with inversion recovery) fat suppression pulse. In addition, a dual-TR (Yarnykh, 2007)  $B_1$ -mapping sequence (FOV=205(AP)x179(RL)x132(FH) mm<sup>3</sup>, FA= $60^\circ$ , TR<sub>1</sub>=23 ms, TR<sub>2</sub>=103 ms, TE=5 s, acquisition bandwidth= 4271 (Hz),  $3.2 \times 3.2 \times 4$  mm<sup>3</sup> resolution, 3 min 3 s acquisition time) was used to measure the  $B_1$ -field distribution. A further experiment was performed in one sub-

ject where data were acquired with a set of SPIR pulses of nominal FA=[ $0^\circ$ ,  $30^\circ$ ,  $45^\circ$ ,  $60^\circ$ ,  $78^\circ$ ,  $90^\circ$ ]. In addition, for a FA= $90^\circ$  two data sets were acquired, one in which the SPIR pulse was applied prior to each RF acquisition and one in which a SPIR pulse was applied prior to every alternate RF acquisition (hence using 50% of the number of FS pulses).

The measured longitudinal relaxation rate  $R_1(r)$  was modelled as a weighted sum of the relaxation rates due to macromolecular relaxation and its modulation by the fat suppression pulses, which is a function of the nominal flip angle of the SPIR fat suppression pulse, FA, the RF field distribution,  $X(r)$ , and myelin density  $m(r)$ :

$$R_1(r) = a \cdot m(r) + b \cdot FA \cdot X(r) \cdot m(r) \quad (1)$$

where  $a$  and  $b$  are constants. This model assumes that (i) the longitudinal relaxation of water protons in brain tissue is mono-exponential (in agreement with Rioux et al. (2016), which shows that the contribution from myelin water is very small and quickly decays before the shortest TI used in this study), (ii) lipid membranes, especially myelin, dominate the longitudinal relaxation and magnetization transfer of water proton spins in brain tissue, both in white matter and in cortical grey matter, and ignores the effect of iron on the longitudinal relaxivity and (iii) additional RF pulses (e.g. from fat suppression pulses) increase the longitudinal relaxation rate in water protons due to magnetization transfer from lipid membrane molecules (Kucharczyk et al., 1994).

A linear fit of  $R_1(r)$  versus  $FA \cdot X(r)$  was performed to estimate  $\alpha = a \cdot m(r)$  and  $\beta = b \cdot m(r)$  from a least-squares regression, and thus evaluate the constant  $(b/a)$  for each voxel of the brain. This constant was then used to form a corrected  $R_1$  map ( $R_{1,corr}$ ), by removing the contribution of magnetization transfer arising from a SPIR fat suppression RF pulse with amplitude FA:

$$R_{1,corr}(r) = \frac{R_1(r)}{\left(1 + \frac{b}{a} \cdot FA \cdot X(r)\right)} \quad (2)$$

Corrected  $R_1$  maps were generated in two ways, using a voxel specific ( $b/a$ ) parameter (voxel-wise correction) or using a constant ( $b/a$ ) value for every voxel (global correction), defined by the peak of the histogram given by the distribution of  $b/a$  values across the entire brain.

### 2.5.3. Comparison of MS-IR-EPI with MP2RAGE and single slice IR-EPI

Whole head images were obtained at 7 T, with 0.7 mm isotropic resolution (Table 1: protocols MS1 (SMS=2) and MP1) and at 3 T, with 1 mm isotropic resolution (Table 1: protocols MS5 (SMS=2) and MP3). These were compared with MP2RAGE  $T_1$  maps corrected for  $B_1$ -inhomogeneities, and  $T_1$  maps obtained using a single slice IR-EPI acquisition (0.7 mm isotropic resolution, TR=5 s, EPI factor=15, TE=15 ms) repeated for multiple inversion times (TI(ms)=[305, 600, 930, 1555, 2180, 2805, 3430, 4055]) in a 4 min 50 s acquisition time.

Five subjects were scanned at 7 T. A SPIR fat suppression FA=70° pulse was applied, and a global ( $b/a$ ) correction of the  $T_1$  maps performed to remove MT effects due to the FS pulses. An additional acquisition using a SPIR fat suppression FA=40° pulse was performed for Subjects 4 and 5, who did not participate in the experiment to model the impact of FS pulses (see Section 2.2.1), to compute subject-specific global ( $b/a$ ) parameters (see Supplementary material).

In order to evaluate the SNR per unit time of  $T_1$  maps derived from the MS-IR-EPI and MP2RAGE sequences, the MP2RAGE and MS-IR-EPI protocols were repeated on Subject 1 at 7 T. In addition to the whole head MS-IR-EPI protocol (SMS=2, FS pulses on), additional pairs of MS-IR-EPI acquisitions were performed using SMS=1 (two repeats with and without FS pulses).

### 2.5.4. Pushing the spatial resolution of MS-IR-EPI at 7 T

To demonstrate the potential of MS-IR-EPI for high spatial resolution  $T_1$  mapping, a 0.5 mm isotropic resolution sequence with whole head coverage (FOV=164(RL)x192(AP)x168(FH) mm<sup>3</sup>) was implemented at 7 T (Protocol MS3 in Table 1) with 240 slices (SMS=3) and SPIR fat suppression FA=90°. Data were acquired with 10 slice offsets, yielding a total acquisition time of 18 min 22 s. To further highlight the potential of  $T_1$  mapping for cortical parcellation, the visualization of the stria of Gennari corresponding to layer IV of the primary visual cortex was compared for  $T_1$  maps derived using MS-IR-EPI and MP2RAGE data acquired with  $0.35 \times 0.35 \times 0.7$  mm<sup>3</sup> spatial resolution collected in a coronal-oblique orientation perpendicular to the calcarine sulcus. Data were acquired at 7 T using a high density 32-channel surface receiver coil array (MR Coils, Utrecht) positioned over the visual cortex. MS-IR-EPI data (protocol MS4 in Table 1, FOV=128(RL)x80(FH)x24.5 mm<sup>3</sup>, SPIR fat suppression FA=60°) comprised 35 slices. Data were acquired with 5 slice offsets (5 TIs) with 3 repeats of each offset, resulting in a total scan time of 11 min 8 s. An MP2RAGE acquisition (protocol MP2 in Table 1) was performed with the same slice prescription as the MS-IR-EPI (FOV=128 × 80 × 38.5 mm<sup>3</sup>, phase encoding in RL direction, acquisition time = 12 min 8 s). Notice these  $T_1$  maps were not corrected for MT effects of the fat suppression pulses, as their spatial fidelity rather than their quantitative precision was key here. Similarly, MP2RAGE data were not corrected for  $B_1$ + profile inhomogeneities in this comparison.

$T_1$  maps for MS-IR-EPI and MP2RAGE acquisitions over the visual cortex were generated both before and after denoising, using a local complex principal component analysis (LCPCA) technique (Bazin et al., 2019). For the MS-IR-EPI, the three individual data sets acquired with the same slice offset were motion corrected using AFNI's 3dAllineate command (using mutual information as the cost function and with the centre of mass calculation restricted to within the slice plane). Motion parameters estimated using the 'denoised' modulus data were applied to real and imaginary original and denoised data and then averaged prior to applying  $T_1$ -fitting algorithm.

To plot the cortical profiles of the  $T_1$  maps (and  $S_0$  maps for MS-IR-EPI), all maps were re-sampled to an in-plane resolution of  $0.11 \times 0.11$  mm<sup>2</sup> using nearest neighbour interpolation;

FSL's FAST algorithm was run on the re-sampled 'de-noised'  $T_1$  maps to provide WM/GM and GM/CSF boundaries which were then used to derive 20 cortical depths using the equivolume approach (Wachnert et al., 2014) implemented in the LAYNII software (<https://doi.org/10.5281/zenodo.3514297>). This cortical depth segmentation was used to bin  $T_1$  (and  $S_0$ ) values into specific cortical depths.

## 3. Results

### 3.1. Optimisation of the number of acquisitions (TI values) for MS-IR-EPI $T_1$ mapping

The effect of the number of acquisitions used to derive the  $T_1$  maps using a TR of 5 s is shown in Fig. 2. A Monte Carlo simulation (Fig. 2A) showed that the accuracy of the fitted  $T_1$  is independent of the number of TIs used in the fit for greater than 4 TIs chosen, but that the standard deviation of the fitted  $T_1$  varies across slices. As the number of TIs used to derive  $T_1$  decreases, and with fewer permutations the minimum TI will vary significantly by slice, the variation in the standard deviation across slices increases, which can be visualized as 'banding' in the 3D reconstruction of the  $T_1$  map generated using 4 TIs but not for maps generated using 8 TIs, as shown in Fig. 2B, the effect is also less pronounced for a higher SNR level (dash lines).

### 3.2. Validation of $T_1$ mapping methods on the calibrated NIST $T_1$ -spheres

Supplementary material Tables 1 and 2 provide the mean  $T_1$  values measured in the NIST  $T_1$  and  $T_2$  spheres at 3 and 7 T for each  $T_1$  mapping method, along with their respective NiCl<sub>2</sub> and MnCl<sub>2</sub> concentration and reference 3 T  $T_1$  values provided by ISMRM/NIST.

Fig. 3A plots  $T_1$  values measured at 3 T for the single slice IR-TSE, MS-IR-EPI and MP2RAGE sequences against the reference  $T_1$  value for the  $T_1$ -spheres and  $T_2$ -spheres. For the  $T_1$ -spheres, the maximum deviation from the NIST reference  $T_1$  values was 4.7% (sphere  $T_{1\_2}$ ) for IR-TSE, and 5.1% (sphere  $T_{1\_3}$ ) for MS-IR-EPI, while for MP2RAGE the accuracy was 17.3% for sphere  $T_{1\_5}$ , but 8% or better for the other spheres. The mean temperature of the  $T_1$ -spheres phantom was  $21.2 \pm 0.4$  °C and  $20.0 \pm 1.3$  °C for the  $T_2$ -spheres phantom. Linear regression analysis of the different  $T_1$  measures versus the reference  $T_1$  values showed a very strong linear correlation ( $1.003x - 17.2$ ,  $R^2=0.9976$  for IR-TSE;  $1.010x + 6.4$ ,  $R^2=0.9976$  for MS-IR-EPI;  $0.992x - 25.6$ ,  $R^2=0.9962$  for MP2RAGE) for the  $T_1$  spheres. For the  $T_2$ -spheres (right),  $T_1$ -measurements were shorter than the NIST reference  $T_1$  values, particularly for the MP2RAGE measurement of sphere  $T_{2\_1}$  (24% shorter compared to 10% and 7.6% for IR-TSE and MS-IR-EPI respectively). The accuracy was better than 9% for all spheres when using MS-IR-EPI. Since  $T_{2\_10}$  was below 300 ms (hence below the range of  $T_1$  in human brain at 3 T), this sphere was excluded from further analysis. Linear regression had a strong linear correlation ( $0.924x - 33.6$ ,  $R^2=0.9993$  for IR-TSE;  $0.9296x + 13.2$ ,  $R^2=0.9996$  for MS-IR-EPI;  $0.8294x + 96.3$ ,  $R^2=0.9463$  for MP2RAGE) for the  $T_2$ -spheres.

At 7 T, the average single slice IR-EPI  $T_1$  was used as the reference to compare  $T_1$  values from MS-IR-EPI and MP2RAGE methods (Fig. 3B(i)). Measured  $T_1$  values at 7 T were shorter than at 3 T for the NiCl<sub>2</sub>-doped  $T_1$ -spheres, whilst measured  $T_1$  values of the MnCl<sub>2</sub>-doped  $T_2$ -spheres were slightly longer at 7 T ( $\sim 3 \pm 1\%$  for the single slice IR measurement) than at 3 T. In general, MS-IR-EPI slightly overestimates  $T_1$  across all spheres, but accuracy is better than 5% for all spheres except the three  $T_2$ -spheres with shortest  $T_1$  values. MP2RAGE  $T_1$  measurements in these spheres with short  $T_1$ -values are also overestimated by more than 5%, while spheres with the longest  $T_1$  values ( $T_{2\_1}$ ,  $T_{2\_2}$  and  $T_{1\_1}$ ) are underestimated by  $\sim 14\%$ ,  $7\%$  and  $8\%$  respectively, showing poor accuracy compared with MS-IR-EPI (3.2%, 3.5% and 0.5% respectively for these spheres). The mean temperature of the  $T_1$ -spheres phantom was

$20.5 \pm 1.3$  °C and the  $T_2$ -spheres phantom was  $20.4 \pm 0.9$  °C. The repeatability of  $T_1$  measurements is characterized as the CoV (Fig. 3B(ii)). The CoVs of  $T_1$  values were smaller for the  $T_1$ -spheres than for the  $T_2$ -spheres, and those measured with single slice IR-EPI was lowest: < 2.8% for every  $T_2$ -sphere except  $T_{2-6}$  (3.4%), while the CoV for the  $T_1$  spheres was 2.2% ( $T_{1-3}$ ) or less. For MS-IR-EPI, the highest CoV was measured for spheres  $T_{2-9}$  (6.1%) and  $T_{1-5}$  (4.3%), but for  $T_{1s} > 400$  ms the CoV was below 3.5%. The CoV of  $T_1$  values measured with MP2RAGE was the largest, larger than 5% for several  $T_2$ -spheres ( $T_{2-2}$ ,  $T_{2-3}$ ,  $T_{2-4}$ ,  $T_{2-5}$ ,  $T_{2-8}$ ), and the largest CoV was 3.6% ( $T_{1-6}$ ) for the  $T_1$ -spheres.

In order to determine the relaxivity of  $\text{NiCl}_2$  and  $\text{MnCl}_2$  at both field strengths, the longitudinal relaxation rates ( $R_1$ ) measured with each  $T_1$  mapping method were linearly fit versus the  $\text{NiCl}_2$  (for the  $T_1$ -spheres phantom) and  $\text{MnCl}_2$  (for the  $T_2$ -spheres phantom) nominal concentrations. Spheres  $T_{2-2}$ ,  $T_{2-9}$  and  $T_{2-10}$  were excluded from the fit, given the poor accuracy for MP2RAGE measurements (Fig. 3B(i)), spheres  $T_{2-1}$  and  $T_{2-5}$  were also excluded given the unknown  $\text{MnCl}_2$  concentration for these spheres (see Methods). Plots for MS-IR-EPI sequence are shown in Fig. 3C (for the other sequences see supplementary material). The  $\text{NiCl}_2$  relaxivity at 3 T was found to be  $0.66 \pm 0.01$  ( $R^2=0.9999$ ),  $0.63 \pm 0.01$  ( $R^2=0.9997$ ) and  $0.65 \pm 0.01$  ( $R^2=0.9529$ )  $\text{s}^{-1}\text{mM}^{-1}$  using single slice IR-TSE, MS-IR-EPI and MP2RAGE respectively, whereas at 7 T the  $\text{NiCl}_2$  relaxivity was measured to be  $0.86 \pm 0.01$  ( $R^2=0.9999$ ),  $0.81 \pm 0.01$  ( $R^2=0.9998$ ) and  $0.79 \pm 0.01$  ( $R^2=0.9997$ )  $\text{s}^{-1}\text{mM}^{-1}$  respectively. For  $\text{MnCl}_2$ , similar relaxivity values were obtained at 3 T and 7 T;  $8.20 \pm 0.34$  ( $R^2=0.9997$ ) and  $7.96 \pm 0.33$  ( $R^2=0.9999$ )  $\text{s}^{-1}\text{mM}^{-1}$  for single slice IR-TSE (EPI),  $7.10 \pm 0.36$  ( $R^2=0.9999$ ) and  $7.29 \pm 0.34$  ( $R^2=0.9999$ )  $\text{s}^{-1}\text{mM}^{-1}$  for MS-IR-EPI, and  $9.42 \pm 0.23$  ( $R^2=0.9981$ ) and  $7.00 \pm 0.39$  ( $R^2=0.9999$ )  $\text{s}^{-1}\text{mM}^{-1}$  for MP2RAGE.

### 3.3. Effect of TR, SMS factor and number of slices on MS-IR-EPI $T_1$ mapping measurements at 7 T

Fig. 4A shows the  $T_1$  histogram generated from data acquired with (dash lines) and without (solid lines) SMS for a TR of 5 s (blue) and 3.2 s (red). The  $T_1$  histograms for data acquired with SMS=1 and SMS=2 (TR=5 s) are very similar, whilst the  $T_1$  histogram for data acquired with SMS=3 is broader than that for the SMS=1, with a slightly lower peak for GM. Data acquired with SMS=1 shows that the reduced TR of 3.2 s (solid lines) yields shorter  $T_1$  values than for a TR of 5 s, particularly for GM. Fig. 4B shows that the  $T_1$  histograms are very similar for a central slice of the MS-IR-EPI acquisition (TR=3.2 s (SMS=1)) acquired with a different number of slices and a single slice IR-EPI data set.

### 3.4. Effect of fat suppression pulses on $T_1$ measurements

The model of the effect of fat suppression on longitudinal relaxation rate (Eqn.(1)) assumes the longitudinal relaxation of water protons in brain tissue is mono-exponential, whether or not there is further relaxation due to magnetization transfer. Logarithmic plots of the MS-IR-EPI signal intensity (within a ROI in the corpus callosum) versus inversion time indeed show a very strong linear relation ( $R^2 > 0.99$ ) for each of the data sets acquired with different fat suppression levels (Fig. 5A). There is also a strong linear correlation of the fitted  $R_1$  values versus fat suppression SPIR flip angle ( $R^2=0.9954$ ) (Fig. 5A inset). Fig. 5B shows a histogram of the  $b/a$  parameter obtained by voxel-wise linear regression of  $R_1$  versus SPIR FS flip angle for GM (dark grey), WM (light grey) and total (WM+GM) tissue (black) for the three subjects scanned. The distribution of  $b/a$  is very similar for GM and WM, hence the distribution of total GM and WM tissue values across the brain was fit to a two Gaussian mixture model (red line), and the mode of highest amplitude Gaussian used as a constant parameter for the global correction method; this was found to be very similar across subjects (with a mean value of  $0.0045 \pm 0.0002 \text{ s}^{-1}$ ). The voxel-wise correction introduces propagated noise in the corrected  $R_1$  maps. Given that the measured voxel-wise  $b/a$  correction factor shows a very slow spatial variation compared

with structural details, we were able to improve the SNR of the corrected  $R_1$  maps when using the voxel-wise correction by spatially smoothing the  $b/a$  parameter maps with a 2 mm Gaussian kernel. Larger kernels did not further reduce the standard deviation in the corrected  $R_1$  maps.

The default RF power for the ‘strong’ SPIR fat suppression pulse in the Philips system corresponds to a FA of 120°, with a FA of 90° assigned to ‘medium’ and 60° to ‘weak’ power respectively. For the whole-head MS1 protocol (Table 1), these pulse strengths result in SAR levels of 1.5, 2 and 2.7 W/Kg respectively. We observed that a SPIR fat suppression pulse with FA of 70° was sufficient to effectively suppress the fat artefact with 19.2 FS pulses per second (Fig. 6). This resulted in a 41% reduction in the SAR level of the sequence compared to the default ‘strong’ FS power. Fig. 6A shows that the position of the peak of the  $R_1$  histogram increases as the SPIR fat suppression flip angle increases (solid colour lines) as compared to no fat suppression (black line). Table 3A summarises the  $T_1$  values at the histogram peaks in GM and WM for data acquired with no fat suppression and with 70° flip angle SPIR pulses. When we used 70° flip angle SPIR pulses, GM  $T_1$  values were shortened by 17% (Subject 3) to 23% (Subject 1) and WM  $T_1$  values by 21% (Subject 2) to 25% (Subjects 1), compared with no fat suppression.  $R_1$  maps collected across SPIR flip angles were linearly fit to Eq. (1) to generate a  $b/a$  parameter map. Histograms of  $R_1$  maps corrected (Eq. (2)) using the voxel-wise method are shown in Fig. 6Ai, whilst Fig. 6Aii (and 6Aiii) show  $R_1$  histograms corrected using a constant  $b/a$  parameter value (global correction). The  $R_1$ -corrected histograms (dash lines) are similar across fat suppression levels and match the data acquired with no fat suppression (black line), with a narrower distribution (smaller FWHM and higher peak) than the uncorrected data, particularly for the global correction method (see Table 3 for measures for the data acquired with FS flip angle of 70°). The histogram peaks for the  $R_1$ -corrected data are closer to the reference (no fat suppression data), with slightly longer  $T_1$  values 7.1 and 5.6% of (GM) and 10.7 and 3.5% (WM) (across subjects) for voxelwise and global correction respectively. The use of a reduced dataset of two  $R_1$  maps with SPIR FAs of 40° and 70° to derive the global  $b/a$  correction parameter yields results (Fig. 6Aiii) very similar to the full data set (Fig. 6Aii). The maximum difference in corrected- $R_1$  (compared to correction using the full data set) was 1.8% for GM and 1.1% for WM in Subject 2 (Table 3).

Fig. 6Bi shows the similarity of the voxel-wise  $b/a$   $R_1$ -corrected maps (second row) with  $R_1$  map after correction with a global constant  $b/a$  (third and fourth rows for regression using data with 5 and 2 FS flip angles respectively). The corrected  $R_1$  maps are generally similar to those acquired with no fat suppression (no-FS, Fig. 6Bii). The global correction shows smaller variance than the voxel-wise correction, appearing similar to the no-FS map but with the fat artefact removed. Table 3A shows that the  $T_1$  values obtained with both correction methods are similar, although slightly longer for the voxel-wise  $b/a$  correction method, particularly for WM (maximum difference of 3.4% for GM and 7.7% for WM in Subject 1). The  $R_1$  histograms for the global correction display a higher peak and narrower FWHM, reflecting the increased SNR compared to the voxel-wise method. It should be noted, however, that when a  $B_1$ -map is unavailable the voxel-wise method can be used to remove spatial variations due to both an inhomogeneous RF transmit field and attenuation of the water signal by the spectrally selective FS pulses in areas of inhomogeneous  $B_0$  (see Supplementary Material, Fig. 4). Effective correction can also be achieved by collecting two data sets with FS flip angle (90°), but where data are collected with an FS pulse prior to each acquisition in one map and prior to alternate acquisitions in the other map, such that MT effects are exactly halved.

### 3.5. Comparison of MS-IR-EPI with MP2RAGE and single slice IR-EPI $T_1$ mapping

$T_1$  histograms of a single slice are shown in Fig. 7Ai with distinct WM and GM peaks. Compared to a multi-shot single slice IR-EPI (black line), the GM peak is similar for no FS (light blue) and after correction

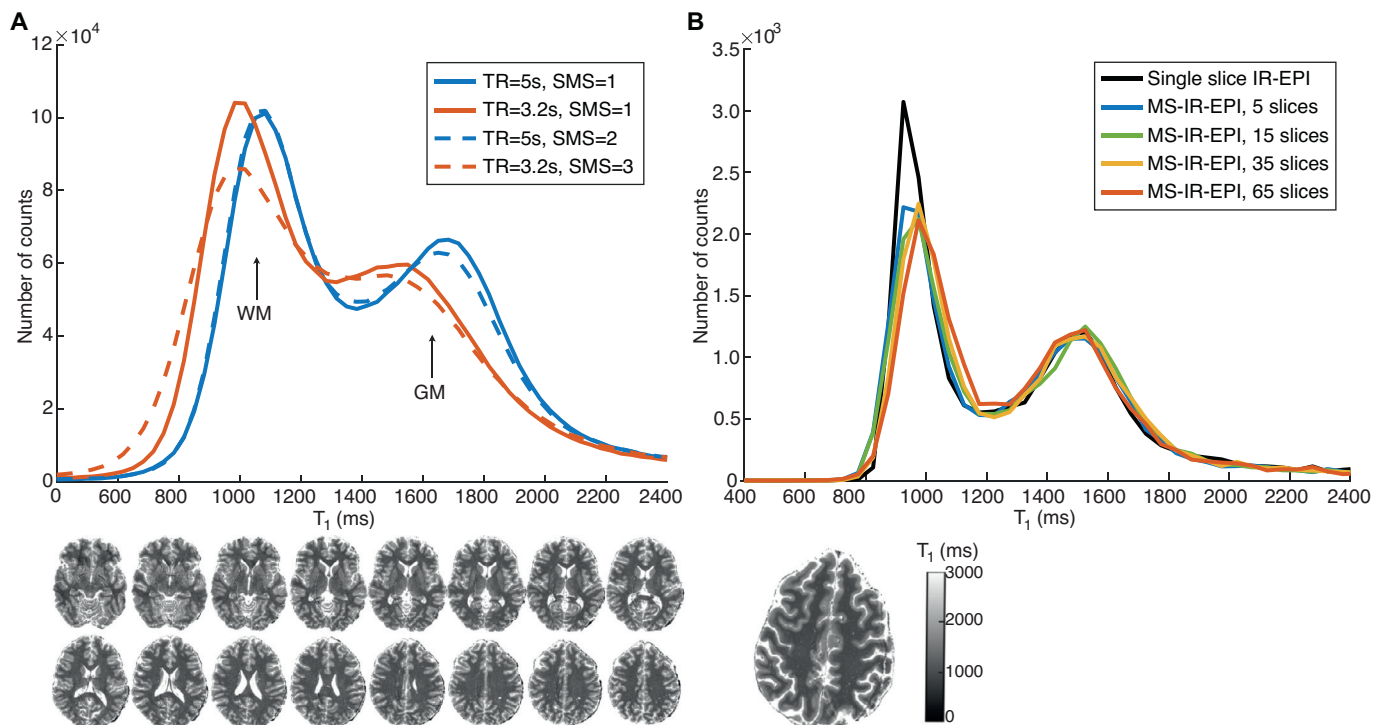


**Fig. 4.** (A)  $T_1$  histograms comparing MS-IR-EPI data acquired with a repetition time (TR) of 5 s (blue solid line, 96 slices acquired) and 3 s (solid red line, 64 slices acquired) with simultaneous multi-slice (SMS) = 1. The dash lines show corresponding  $T_1$  histograms acquired with SMS=2 to acquire 192 slices with TR=5 s (dash blue line) and SMS=3 to acquire 195 slices with TR=3.2 s (dash red line). All histograms correspond to the central imaging volume comprising 64 slices.  $T_1$  maps for every other 4 slices in this volume (acquired with TR=5 s, SMS=1) are shown at the bottom. (B)  $T_1$  histograms from MS-IR-EPI (TR=3.2 s, 5TIs, SMS=1) datasets acquired with a different number of slices (red: 65 slices; yellow: 35 slices; green: 15 slices and blue: 5 slices) compared to a single slice IR-EPI acquisition with matched scan parameters (TIs=[320 900 1470 2050 2625]ms). All histograms from MS-IR-EPI data correspond to the central slice, matching the single slice IR-EPI shown in the figure. (For interpretation of the references to colour in this figure legend, the reader is referred to the web version of this article.)

**Table 3**

$T_1$  values of histogram peak for data acquired with standard single slice IR-EPI, MS-IR-EPI with fat suppression (both same slice as the standard IR-EPI and whole brain) and whole brain MP2RAGE.

$T_1$ (ms)		Subject 1	Subject 2	Subject 3	Subject 4	Subject 5	Mean $\pm$ std
Single slice	GM	1790	1730	1688	1762	1758	1746 $\pm$ 39
IR-EPI	WM	1010	1090	1083	1108	1092	1077 $\pm$ 38
MS-IR-EPI	GM	1766	1790	1798	1770	1828	1790 $\pm$ 25
(single slice)	WM	1077	1170	1176	1158	1168	1151 $\pm$ 42
MS-IR-EPI	GM	1690	1766	1806	1845	1808	1783 $\pm$ 60
(whole brain)	WM	1110	1155	1200	1195	1192	1170 $\pm$ 38
MP2RAGE	GM	1641	1615	1635	1685	1688	1653 $\pm$ 32
(whole brain)	WM	1100	1135	1145	1155	1165	1140 $\pm$ 25

(dark blue), but the WM peak  $T_1$  is longer for the corrected  $R_1$  sequence (see Table 3: across subjects the  $T_1$  values for MS-IR-EPI are longer than a single slice IR-EPI by 1.6% and 6.3% in GM and WM respectively). MP2RAGE gives a WM peak  $T_1$  similar to MS-IR-EPI (with FS) whereas the GM peak is shorter. This pattern is repeated for the whole brain volume (Table 3), with mean WM  $T_1$  of 1170 $\pm$ 38 ms and 1140 $\pm$ 25 ms measured with MS-IR-EPI and MP2RAGE sequences respectively ( $n = 5$ ), and mean GM  $T_1$  of 1783 $\pm$ 60 ms for MS-IR-EPI compared to 1653 $\pm$ 32 ms for MP2RAGE. Fig. 7Aii compares  $T_1$  maps generated with MS-IR-EPI and MP2RAGE in axial, sagittal and coronal views. The red arrow indicates the effect of the large  $B_0$  field gradient in regions near air-tissue interface, causing larger distortions in MS-IR-EPI than MP2RAGE.

The SNR-per-unit-time for MS-IR-EPI and MP2RAGE measures of  $T_1$  at 7 T in the NIST/ISMRM spheres and *in-vivo* are shown in Fig. 7Bii. Data for the phantom shows the SNR-per-minute is higher for MS-IR-EPI (blue) than MP2RAGE (red) in all spheres, particularly for the TR=3.2 s protocol. Also note that the SNR per unit time is only slightly decreased when using SMS=2 compared to SMS=1. In contrast, SNR-per-minute in

the brain (Fig. 7Bi) is larger for  $T_1$  in GM tissue measured with MS-IR-EPI for SMS=1 but is reduced below the level of MP2RAGE when using SMS=2 with FS and for all MS-IR-EPI measures in WM.

### 3.6. Pushing the spatial resolution of MS-IR-EPI at 7 T

High spatial resolution ( $0.35 \times 0.35 \times 0.7$  mm<sup>3</sup>)  $T_1$  maps of the visual cortex generated with MS-IR-EPI and MP2RAGE are shown in Fig. 8A. The arrows indicate the presence of a hypointense band within the calcarine sulcus corresponding to the Stria of Gennari. This can be observed in  $T_1$  maps generated with MP2RAGE (top row) and MS-IR-EPI (middle row), as well as in the  $S_0$  parameter fit for MS-IR-EPI (bottom row). The visual appearance of the MP2RAGE data is in line with previous work (see Waehnert et al., 2016) in which the Stria of Gennari is typically only sporadically visible, this is also the case for the MS-IR-EPI data (Fig. 8A(i)). Intracortical profiles from WM to the CSF boundary are plotted for striate and extra-striate cortex (for the original data before de-noising) in Fig. 8B, showing a clear mid-cortical dip in  $T_1$  and  $S_0$

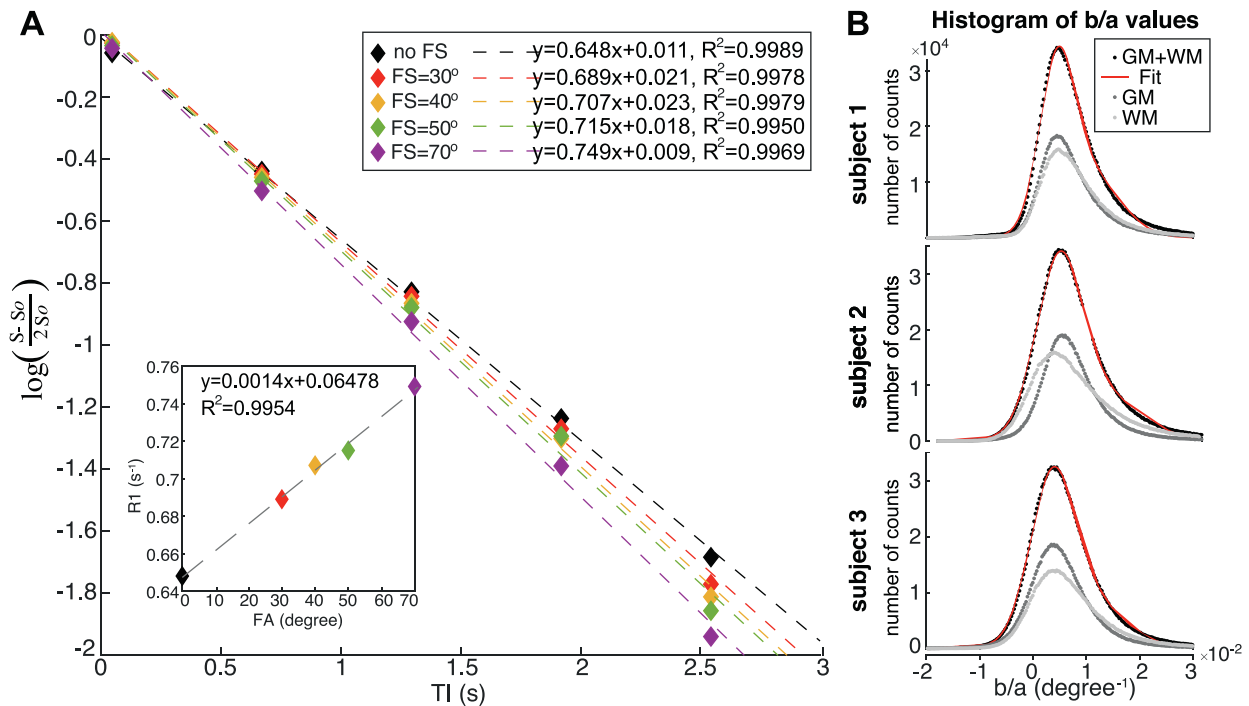


**Fig. 5.** (A) Logarithmic plot of the signal intensity within a region of interest in the corpus callosum (single slice, subject 2) versus inversion time for data acquired measured for a MS-IR-EPI dataset with no fat suppression (black diamonds) and with different fat suppression (FS) SPIR pulse flip angle (coloured diamonds). The logarithmic y-axis plots the difference in signal intensity ( $S$ ) at each of the first 5 inversion times compared to the last inversion time ( $S_0$ ). The dash lines plot the linear fit for each data set, showing strong linearity ( $R^2 > 0.99$ ). Each fit's gradient corresponds to the longitudinal relaxation rate ( $R_1$ ) which increases with increasing fat suppression power. The inset shows that the fitted  $R_1$  is linearly correlated with the SPIR pulse flip angle. (B) Histogram of  $b/a$  parameter values obtained by linear regression of  $R_1$  versus SPIR FS flip angle for GM tissue (dark grey), WM tissue (light grey) and total (GM+WM) tissue (black) for each subject. Red line: double Gaussian fit to the (GM+WM) data. (For interpretation of the references to colour in this figure legend, the reader is referred to the web version of this article.)

values for the MS-IR-EPI data within striate cortex compared to extrastriate cortex, but not in  $T_1$  values from the MP2RAGE data. The  $S_0$  image from the MS-IR-EPI data is also of notably very high quality, and may aid the definition of intracortical veins. Due to the MS-IR-EPI data exhibiting reduced blurring, after complex denoising (Fig. 8A(ii)) the visualization of the Stria of Gennari is improved for MS-IR-EPI data but not for MP2RAGE data. Fig. 8C shows whole head 0.5 mm isotropic  $T_1$  maps generated with MS-IR-EPI in under 19 min (note these data have not been de-noised).

#### 4. Discussion

We have implemented a fast multi-slice multi-shot inversion-recovery 2D-EPI  $T_1$  mapping method, which completely fills the time available after each inversion pulse with acquisition of k-space segments of each slice, minimizing any dead-time and limits geometric distortions and image blurring. We combined this sequence with slice offset sampling and simultaneous multi-slice imaging to generate time-efficient  $T_1$  maps of the whole brain with sub-millimetre spatial resolution. Monte Carlo simulations allowed the minimum number of acquisitions needed to obtain consistent  $T_1$  values across slices to be determined. Banding in the slice direction may originate from phase errors in regions where the longitudinal magnetization is near zero. Simulations show that as the number of TIs and SNR increases the 'banding artefact' becomes less prominent (Fig. 2A(ii)). Cohen and Polimeni (2017) have shown that the slice ordering can also be optimized to reduce the required number of measurements without adversely affecting the quantitative accuracy and precision of the  $T_1$  maps.

The MS-IR-EPI results were compared with those using a single slice IR-EPI sequence and the widely used 3D MP2RAGE  $T_1$  mapping with  $B_1$ -correction (Marques et al., 2010; Van de Moortele et al., 2009; Haast et al., 2018; Marques and Gruetter, 2013). The MS1 protocol with

TR=5 s is optimal to accurately measure  $T_1$  in the brain at 7 T, whereas for applications where the precision of the  $T_1$  value is not critical, such as cortical depth analysis (Huber et al., 2016; Kashyap et al., 2018) or cortical parcellation where relative changes are important, protocols with shorter TR may be preferred to speed up the acquisition.

##### 4.1. Validation of $T_1$ mapping methods on the calibrated NIST $T_1$ -spheres

$T_1$  values obtained with MS-IR-EPI at 3 T were consistent with the reference  $T_1$  values of the  $T_1$ -spheres ( $R^2=0.9976$ ) and  $T_2$ -spheres ( $R^2=0.9767$ ) provided by NIST. We report, for the first time, quantitative  $T_1$  values of the ISMRM/NIST  $T_1$ -sphere system and  $T_2$ -sphere system at 7 T. At 7 T, both the  $T_1$  mapping accuracy (with respect to the single slice IR measure) and repeatability of MS-IR-EPI were superior to that of MP2RAGE. In particular, for long  $T_1$  values (>1800 ms) MS-IR-EPI provides good accuracy while MP2RAGE underestimates  $T_1$ , suggesting that longer TR<sub>shot</sub> is required for MP2RAGE to accurately measure  $T_1$  in grey matter tissue. The accuracy of both MS-IR-EPI and MP2RAGE decreases for low  $T_1$  values (<500 ms), which are below the physiological range of  $T_1$  in the human brain at 7 T.

It is worth noting that although we show a reduction in the sphere  $T_1$  values at 7 T as compared with 3 T, which at first may seem inconsistent with the commonly expected increase in  $T_1$  with field strength (Yen et al., 2017), we have found that this is a predictable result of the increase of the relaxivity ( $r$ ) of NiCl<sub>2</sub> between 3 T ( $-0.63 \text{ s}^{-1}\text{mM}^{-1}$ ) and 7 T ( $-0.81 \text{ s}^{-1}\text{mM}^{-1}$ ) measured with MS-IR-EPI. This is consistent with previous work showing a relaxivity of NiCl<sub>2</sub> at 7 T of  $0.93 \pm 0.23 \text{ s}^{-1}\text{mM}^{-1}$  (Rooney et al., 2007) compared to lower measures at lower field strengths (ranging from 0.2 to 4T). Our measure of relaxivity at 3 T is also in agreement with previous work reporting an  $r$  of  $0.620 \text{ s}^{-1}\text{mM}^{-1}$  (Thangavel et al., 2017). We found that our measures of relaxivity of MnCl<sub>2</sub> were similar at 3 and 7 T ( $7.10 \pm 0.36$  and  $7.29 \pm 0.34 \text{ s}^{-1}\text{mM}^{-1}$

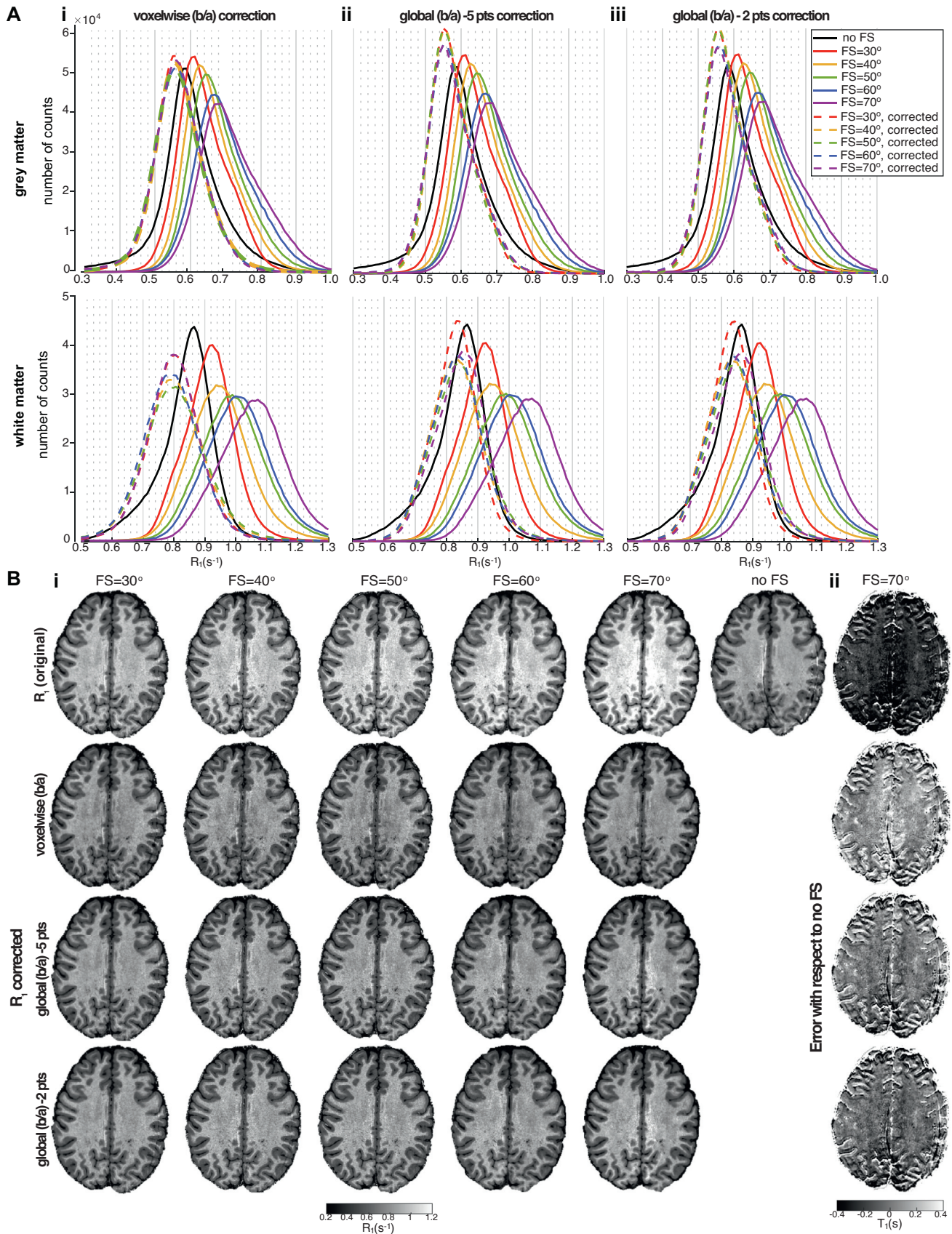


**Fig. 6.** (Ai)  $R_1$  histograms in grey matter (top) and white matter (bottom) for one subject's data acquired with different levels of fat suppression (FS) by varying the flip angle of the SPIR pulse. The black line represents data acquired with no FS and the colour solid lines represent data acquired with FS SPIR flip angles ranging from 30° (red) to 70° (violet). The dashed colour lines show corresponding  $R_1$  histograms after correction using:  $b/a$  data generated by linear regression of  $R_1$  versus SPIR flip angle to correct (Eqn. (2)) using: (i) voxelwise correction (the  $b/a$  parameter map was spatially smoothed by a Gaussian kernel with a full width at half maximum (FWHM) of 2 mm prior to correction) and a global  $b/a$  correction with the constant  $b/a$  parameter value computed from (ii) the full dataset comprising 5 FS flip angles of 30°, 40°, 50°, 60° and 70° and (iii) a reduced dataset of two FS flip angles of 40° and 70° only. (B) (i) Original  $R_1$  maps (first row) shown for the different SPIR flip angles (including data acquired with no fat suppression, right) and corresponding  $R_1$  maps after correction with the different methods. (ii) Difference image between  $T_1$  maps for data acquired with SPIR FA=70° (uncorrected and corrected with the different methods) and data acquired with no FS. (For interpretation of the references to colour in this figure legend, the reader is referred to the web version of this article.)

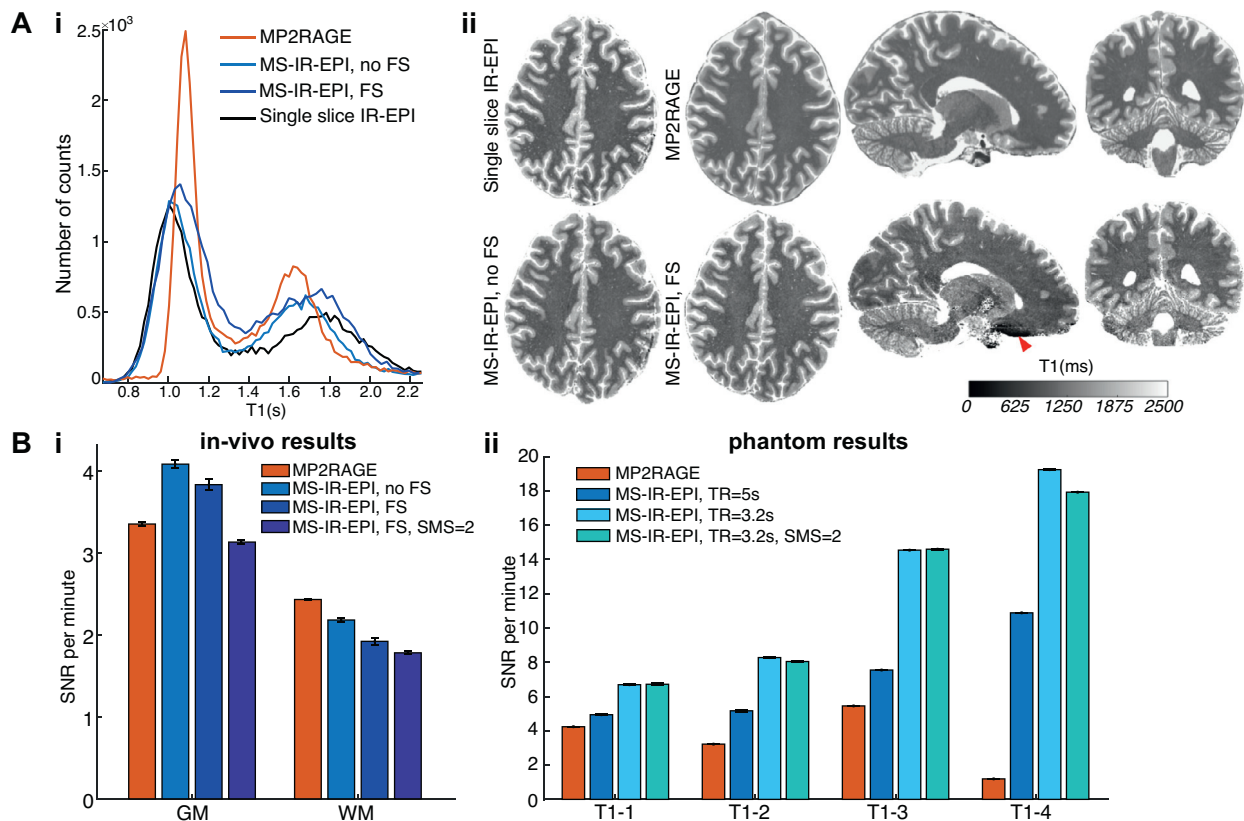


**Fig. 7.** (A) Comparison of  $T_1$  maps obtained with the different schemes at 7T. (i)  $T_1$  histograms for a single slice (shown in ii) for single slice IR-EPI (black line), MP2RAGE (orange) and MS-IR-EPI with (dark blue) and without (light blue) fat suppression. Notice that the data acquired with fat suppression had been corrected as described in the methods. (ii) Comparison of whole brain  $T_1$  maps (sagittal, coronal and axial views) obtained with MP2RAGE (top row) and MS-IR-EPI acquired with fat suppression pulses and SMS=2 (bottom row). Axial view also shown for  $T_1$  map generated with MS-IR-EPI and single slice IR-EPI schemes without fat suppression. (B) SNR per unit time (minute) comparison in (i) GM and WM tissue ROIs for  $T_1$  maps generated with MP2RAGE (orange) and MS-IR-EPI schemes without fat suppression (using SMS=1) pulses and with fat suppression pulses for SMS=1 and SMS=2. (ii) NIST sphere for  $T_1$  maps generated with MP2RAGE (orange) and MS-IR-EPI (different shaded of blue). Errorbars represent the standard deviation across two repeat measurements. (For interpretation of the references to colour in this figure legend, the reader is referred to the web version of this article.)

respectively for MS-IR-EPI) and comparable to  $r$  values for  $\text{MnCl}_2$  reported in the literature:  $6.397 \text{ s}^{-1}\text{mM}^{-1}$  (Thangavel et al., 2017) and  $7.4 \text{ s}^{-1}\text{mM}^{-1}$  (Nofiele and Cheng, 2013) at 3 T, and  $6.37 \text{ s}^{-1}\text{mM}^{-1}$  (Castets et al., 2015) at 7 T. Although the accuracy (with respect NIST  $T_1$  reference values) was better for the  $T_1$ -spheres than the  $T_2$ -spheres, the  $T_2$ -spheres are better suited for 7 T imaging as they offer a wider range of  $T_1$ -values which more closely match those found within the human brain compared to the  $T_1$ -spheres, due to the increased relaxivity of  $\text{NiCl}_2$  at 7 T.

#### 4.2. MT effects on measured $T_1$ values due to spectrally selective fat suppression pulses

MS-IR-EPI data were collected using a range of SPIR fat suppression flip angles. Our results show that spectrally selective fat suppression pulses decrease the apparent value of  $T_1$ , with a severe underestimation when using high power FS pulses (Fig. 6). It has been previously demonstrated using multi-slice Look-Locker imaging (Shin et al., 2009) that frequency-selective fat suppression pulses can invoke magnetization transfer contrast through the exchange between free and motion-restricted protons. Cohen and Polimeni (2018) investigated the effects of the fat suppression pulses in  $T_1$  measurements of the NIST calibrated  $T_1$ -spheres phantom and showed that the  $T_1$  shortening effect of the fat suppression pulse was particularly pronounced for phantom compartments with long  $T_1$ . Although the study by Polders et al. (2012) using single-shot MS-IR-EPI with SPIR fat suppression pulses at 7 T found that

fat suppression pulses did not significantly affect the estimated  $T_1$  values in a human brain, Renvall et al. (2016) showed maps at 3 T with reduced  $T_1$  when fat suppression was applied. This is in line with a more recent study (Kashyap et al., 2018) reporting  $T_1$  values at 7 T using single shot multi-slice EPI with fat suppression pulses (GM:  $1460 \pm 250$  ms, WM:  $970 \pm 150$  ms: comparable to the  $T_1$  values observed in our study with SPIR FA=70°) which were considerably shorter than those measured with MP2RAGE (GM:  $1666 \pm 220$  ms, WM:  $1180 \pm 90$  ms). Note that the degree of reduction in  $T_1$  values may vary across MR vendors as the fat suppression implementation is not identical across vendors. This discrepancy above can be explained by the small number of fat suppression pulses used (4.6 pulses per second) by Polders et al. compared to the Kashyap et al. study (11.7 pulses per second) and the multi-shot MS-IR-EPI sequences used in the present study (19.2 pulses per second for MS1, Table 1). We indeed observed that halving the number of fat suppression pulses in the sequence had a dramatic effect in the measured  $T_1$  values (for high power SPIR pulses, Supplementary Material Figure 4). This is consistent with Shin et al. (2009) who showed that the fractional loss by magnetization transfer effects was more severe for shorter repetition times and a greater slice number.

Shin et al. (2009) suggested the use of water-selective binomial composite pulses to suppress the fat artefact while minimizing MT effects. However, these water-selective binomial pulses are effective only for low flip angles and large slice thicknesses, conditions which are ideal for a Look-Locker sampling scheme and 3D readouts where low flip angles are used, but not useful for high spatial resolution 2D-EPI acquisi-

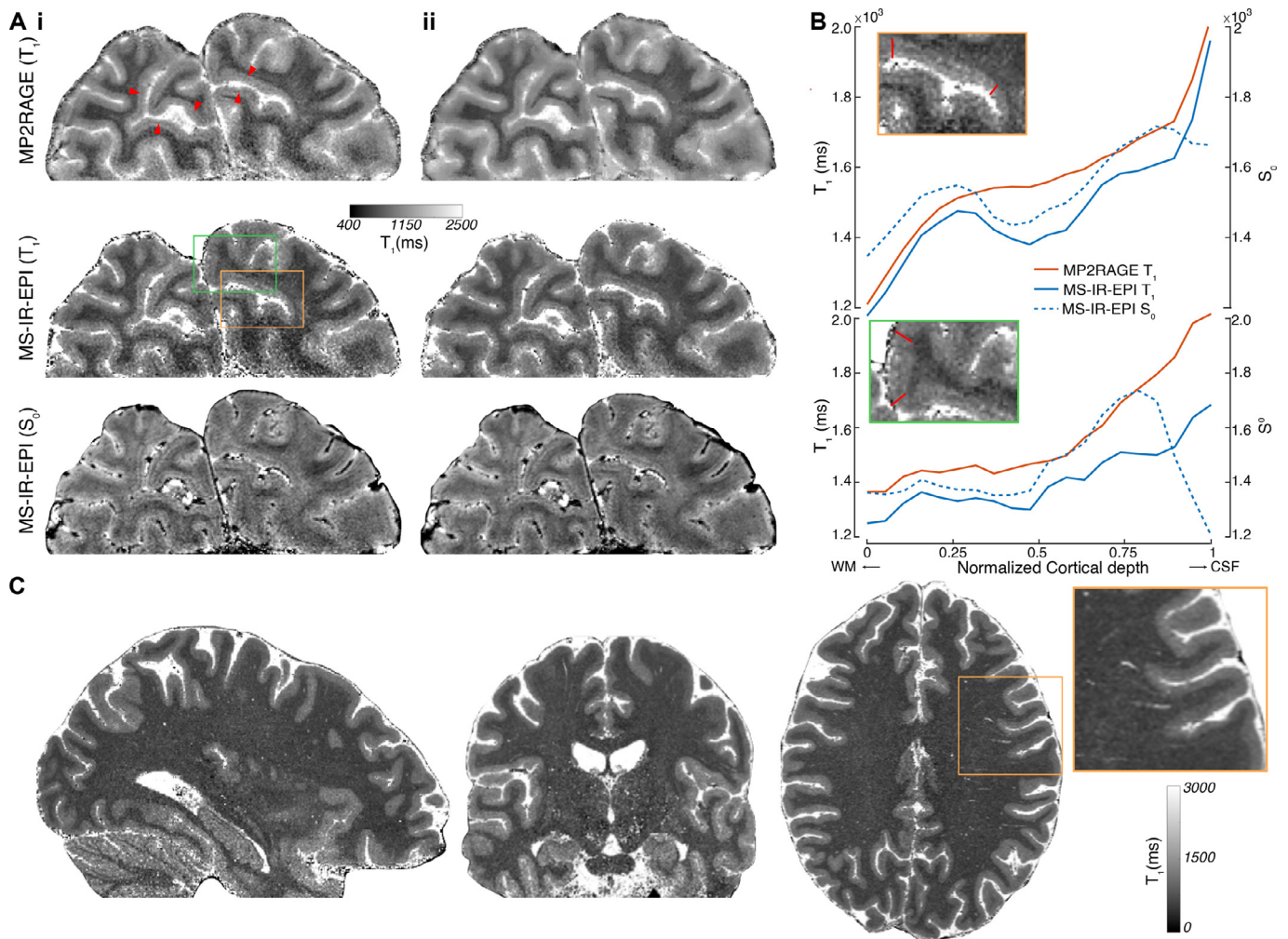


**Fig. 8.** (Ai) High spatial resolution ( $0.35 \times 0.35 \times 0.7 \text{ mm}^3$ )  $T_1$  maps generated from MP2RAGE data ( $T_{1_1}/T_{1_2}=900/2375 \text{ ms}$ ,  $TR_{\text{shot}}=4.5 \text{ s}$ , 55 slices, 12 min 8 s acquisition time; top row) and fitted  $T_1$  (middle row) and  $S_0$  (bottom row) maps derived from MS-IR-EPI data ( $TR=3.2 \text{ s}$ ,  $TE=20 \text{ ms}$ , EPI factor=13, 35 slices, offsets=[0,7,14,21,28], 3 averages, 11 min 8 s total acquisition time) for an example slice of a partial brain dataset. The red arrowheads point to the Stria of Gennari. (ii) Corresponding maps after complex de-noising. (B) Cortical profiles for each of the original data sets (without de-noising) shown in (A) – mean across profiles between the two boundaries indicated by the red lines in the insets (top left) for a region within the striate cortex (top) and a region outside the striate cortex (bottom). Cortical profiles are plotted from the WM boundary to CSF boundary. Profiles from the striate cortex show a dip in  $T_1$  (and  $S_0$ ), corresponding to the Stria of Gennari, for the MS-IR-EPI data (solid and dashed blue profiles, respectively) but not for the MP2RAGE data (orange), whereas profiles outside the Stria do not show a dip. (C) Whole head MS-IR-EPI  $T_1$ -data acquired at 0.5 mm isotropic resolution (EPI factor=7,  $TE=14 \text{ ms}$ ,  $TR=3.8 \text{ s}$ , offsets=[0,8,16, 24, 32, 40, 48, 56, 64, 72], SMS=3, 240 slices, 18 min 44 s acquisition time). (For interpretation of the references to colour in this figure legend, the reader is referred to the web version of this article.)

tions. We also investigated whether magnetization transfer effects due to off-resonance RF irradiation from the slice selective pulses of neighbouring slices had any significant effect on the  $T_1$  value (Santyr, 1993; Wright et al., 2008). Comparison of  $T_1$  maps generated with varying number of slices, in the absence of fat suppression pulses showed that this was not the case (Fig. 4).

To correct  $R_1$  measures for MT effects of the fat suppression pulses, we modelled the measured longitudinal relaxation rate as a function of (i) the myelin density, (ii) nominal flip angle of the spectrally selective FS pulses and (iii) the RF field distribution. Our model assumes that the  $R_1$  of water protons in brain tissue is mono-exponential. Rioux et al. (2016) show this to be valid for TI values much greater than that of the short  $T_1$  component, associated with myelin water (Labadie et al., 2014) of the order of 57 ms. Our MS-IR-EPI sequence does not include inversion times short enough to sample this short  $T_1$  component, and the logarithmic plots of the MS-IR-EPI signal intensity versus inversion time show a very closely linear relation, for a wide range of nominal FS pulse flip angles (Fig. 5A). Note that the mono-

exponential assumption fails at the boundary between tissues, but partial volume effects are alleviated by increasing spatial resolution,

Our correction of  $R_1$  values for MT effects is based on the ratio of  $b/a$  values (Eqn. (1)), which was found to be strikingly similar for GM and WM tissue in all three subjects scanned, in agreement with the linear relaxometry model of Callaghan et al. (2015). We compared two methods of correcting the  $R_1$  maps for MT contribution, a voxel-wise correction using the  $b/a$  parameter map or a global correction using a constant value of  $b/a$  from the peak of the  $(b/a)$  histogram. Both methods worked well (Fig. 6) to correct undesired MT effects in the  $T_1$  quantification and yielded very similar  $T_1$  values for GM (1.1% longer for voxel-wise correction) although  $T_1$  values were slightly longer in WM (6.5%) using the voxel-wise correction (Table 3). Our  $T_1$  values for GM (1794/1814 ms for global and voxel-wise correction) are close to those reported in the literature (Wright et al., 2008; Polders et al., 2012; Dieringer et al., 2014) and to those obtained with single slice IR-EPI (Table 3). Shorter  $T_1$  values (5.6% and 6.8% for global and voxel-wise correction respectively, Table 3) were obtained with the MS-IR-EPI ac-

quisition with no fat suppression. The subject-averaged WM corrected  $T_1$  values ( $1157 \pm 49$  and  $1232 \pm 68$  for global and voxel-wise correction respectively) are in line with values reported in the literature, ranging from 1074/1120 ms measured using MS-IR-EPI (Polders et al., 2012), 1220 ms using MP2RAGE (Metere et al., 2017; Caan et al., 2019) and 1284 ms using IR-SE (Dieringer et al., 2014), but shorter than the long  $T_1$  component (1349 ms) measured with IR-SE (Rioux et al., 2016). Direct comparison of  $T_1$  values measured with MS-IR-EPI and reference IR-EPI in a single slice (for two subjects) largely agree, with very slightly longer  $T_1$  (2.5% and 6.9% in GM and WM respectively) measured with MS-IR-EPI. Thus, the proposed correction method appears to enable accurate  $T_1$  quantification with MS-IR-EPI when using spectrally selective fat suppression pulses.

#### 4.2.1. Global versus voxelwise FS correction

The global  $b/a$  FS correction method produces artefact-free maps, as expected, regardless of the power of the FS pulses used in the  $b/a$  parameter estimation. Since a SPIR FS pulse with  $FA=70^\circ$  is required to completely remove the fat ring image artefact (Fig. 6B), this artefact appears in the correction parameter maps when lower FS pulse values are used in their generation, and hence also in the corresponding  $T_1$  maps when the voxel-wise correction is used. In order to achieve voxel-wise-corrected images free from fat artefact, at least two acquisitions are required, one using the minimum FA for the FS pulse to effectively remove the fat artefact, and a second with a higher FA where the MT effects are very strong (see Supplementary Material, Fig. 4). We found that when only two ( $40^\circ$  and  $70^\circ$ ) of the five FS flip angle datasets are used, very similar mean values for  $R_1$  are obtained (1.2% lower for GM, and 1% lower in WM), indicating that the accuracy of the global correction method is not compromised when fewer datasets are used. This is in contrast with the voxel-wise correction, where fewer data sets results in a wider histogram of  $R_1$  values (see Supplementary Material, Fig. 4), suggesting undesired noise propagation from the fitted  $b/a$  values into the voxel-wise corrected maps. However, the voxel-wise method can remove spatial variations due to inhomogeneous RF transmit field without requiring the acquisition of a separate  $B_1$ -map and can correct for signal attenuating caused by the spectrally selective FS pulses in regions with poor  $B_0$  (see Supplementary Material, Fig. 4).

We recommend the global  $b/a$  correction method as this provides accurate  $T_1$  values while introducing minimal noise into the  $T_1$  maps. This method carries the implicit assumption that the relationship between the longitudinal relaxation described by intrinsic  $T_1$  and the magnetization transfer rate remains constant across healthy brain voxels, which would hold if both  $T_1$  and MT relaxation are indeed dominated by the membrane lipid content of each voxel (essentially the myelin content), rather than by iron or brain proteins for example. This assumption is supported by recent work (Leuze et al., 2017) showing that  $T_1$  and MT become uniform in brain tissue cleared of lipids. Our observation that the mode of the  $b/a$  histograms of grey and white matter are similar in magnitude (Fig. 5B) also supports this assumption.

Given the stability across subjects of the  $b/a$  correction parameter value, the mean value across a group of subjects could be hence used as a MT correction parameter for all acquisitions, once this parameter value has been determined for the desired version of the MS-IR-EPI sequence on a specific MRI scanner. It is important to note however that the age dependency was not explored in this study, and it might be possible that during brain development or ageing the  $b/a$  correction parameter will fluctuate. Hence, when studying different groups of participants, a subject-mean global  $b/a$  value characteristic of the group under consideration may be needed.

#### 4.2.2. Accuracy of $T_1$ mapping using mono-exponential models

There has been much discussion of the accuracy of  $T_1$  measurements.  $T_1$  mapping experiments are typically analysed using a mono-exponential model, thereby assigning a single longitudinal relaxation time constant to the magnetization within the voxel. Accuracy can

of course be affected by the choice of optimal sequence parameters (Weiss et al., 1980), the fitting model (Li et al., 2010) and by slice profile imperfections. It has been suggested, however, that the assumption of mono-exponential signal recovery is itself incorrect. Some authors claim that magnetization transfer between free water protons and macromolecule-bound protons itself introduces a second exponential component (Rioux et al., 2016; Rui et al., 2020) giving rise to the divergence of published  $T_1$  values. The bi-exponential recovery of longitudinal magnetization observed in most tissue types, including WM and GM tissue (Gochberg and Gore, 2007; Prantner et al., 2008) has been attributed to this effect, although the short and long  $T_1$  components are hard to relate to the presumed free water and bound proton pools. The single pool model has been shown not to be fully valid at 3 and 7 T for the relaxation of proton spins in white matter. Work by Labadie et al. (2014) showed unequivocally a short- $T_1$  contribution from myelin water, trapped between the myelin layers wrapping myelinated axons. Later work (Rioux et al., 2016) using IR-TSE imaging to characterize the long and short components of  $T_1$  relaxation in WM agreed with this study, and measured a short component of  $T_1=48$  ms (9%) and  $T_1=57$  ms (13%) at 3 and 7 T respectively. They showed, however, that for sequences that acquire data using multiple inversion times, as performed for the proposed MS-IR-EPI sequence, a mono-exponential model is precise for measuring the long  $T_1$  component.

Interestingly, Rioux et al. (2016) also evaluated the effect of the short  $T_1$  component on  $T_1$  estimation using MP2RAGE, since the signal equations used to convert the intensity of a composite MP2RAGE image into a  $T_1$  value assume a mono-exponential  $T_1$  recovery. They found that the effect of the short  $T_1$  component cannot be mitigated as easily as in sequences which use multiple IRs, with significant differences (90 and 125 ms at 3 and 7 T respectively) with respect to the  $T_1$  long component.

#### 4.3. Comparison of whole brain measures between MS-IR-EPI and MP2RAGE

In comparison with MP2RAGE,  $T_1$  values measured with MS-IR-EPI were similar (2.6% longer) in WM but longer (7.9%) in GM. However, our MP2RAGE  $T_1$  measure for GM ( $1653 \pm 32$  ms, average across 5 subjects) is shorter than reported in other studies using MP2RAGE, where values of 1800 ms (Metere et al., 2017), 1959 ms (Caan et al., 2019) and 1870–1979 ms (Marques et al., 2010) are stated. Only one of these studies (Caan et al., 2019) used the same scanner vendor, but the authors also used a longer  $TR_{\text{shot}}$  (6 s) than the 5 s used in the present study, which could potentially result in longer  $T_1$  estimates. In our study, the 5 s time between inversion pulses was chosen to match the TR for the MS-IR-EPI sequence. A recent study using the same  $TR_{\text{shot}}=5$  s for MP2RAGE reported a very similar  $T_1$  value ( $1660 \pm 35$  ms) for GM tissue to results reported in this manuscript. These observations, taken together with our phantom results suggest that the MP2RAGE sequence underestimates  $T_1$  values  $> 1800$  ms, as a  $TR_{\text{shot}}$  of 5 s is too short to accurately measure GM. In contrast, for the MS-IR-EPI sequence,  $T_1$  could be accurately measured in GM (yielding comparable measures to single slice IR-EPI). It should be noted that the longitudinal magnetization has more time to freely recover in MS-IR-EPI compared with MP2RAGE, where the longitudinal magnetization is continuously sampled over the long GRE trains.

Both MS-IR-EPI and MP2RAGE sequences use adiabatic inversion pulses, which makes these sequences less sensitive to  $B_1$ -field inhomogeneities than other sequences, such as the Variable Flip Angle method (Stikov et al., 2015). Simulations for different levels of the adiabatic inversion on the accuracy of  $T_1$  measured show that for target  $T_1$  value of 2000 ms, the error is only 10.7 ms (0.5%) when the efficiency is 90%, increasing to  $\sim 30$  ms (1.5%) when efficiency is further reduced to 70%, and this error decreases for shorter  $T_1$  targets (see Supplementary Material, Fig. 2). For the MP2RAGE sequence,  $B_1$ -transmit field inhomogeneities cause deviations from the nominal flip angles in the GRE trains, since the longitudinal magnetization is continuously sampled dur-

ing the GRE acquisition train, errors in the FA will affect the accuracy of  $T_1$  estimates. In contrast, for MS-IR-EPI the longitudinal magnetization experiences a single excitation pulse. Deviations from the nominal excitation FA means that the longitudinal magnetization will not be fully saturated, which will have an impact in the SNR. For MS-IR-EPI, the largest impact on  $T_1$  accuracy due to the varying  $B_1$  transmit field is due to the spectrally selective fat suppression pulse, given that there is a strong dependence of  $T_1$  with the fat suppression FA. Hence, when using spectrally selective fat suppression pulses, knowledge of the  $B_1$ -field distribution is crucial when correcting MT effects from the  $T_1$  maps.

The quality of the whole-brain  $T_1$  maps for MS-IR-EPI is similar to that of MP2RAGE (Fig. 7). The MP2RAGE acquisition takes longer, but provides a higher SNR compared to the faster MS-IR-EPI  $T_1$  map, particularly in WM, as evidenced by the sharper histogram peak for MP2RAGE. Multi-shot EPI acquisitions are more robust against  $B_0$  inhomogeneity than single shot EPI because the lower EPI factor entails a short acquisition window, minimizing geometric image distortions and dropouts. However, the large  $B_0$  field gradient in regions near air-tissue interfaces can still cause minor intravoxel signal dephasing and larger distortions in MS-IR-EPI than MP2RAGE. For  $T_1$  mapping of the temporal lobe near the sinus, a shorter echo time is required, which can be achieved by using parallel acquisition or more segments.

We expected the SNR per unit time in MS-IR-EPI to be higher than that of MP2RAGE. The MS-IR-EPI sequence is very time-efficient as the time between each inversion pulse is densely packed with excitation pulses and their acquisition windows, with minimal dead time compared with MP2RAGE, which needs dead time to allow the longitudinal magnetization to recover. In addition, the MS-IR-EPI acquisition uses  $90^\circ$  flip angle excitation pulses, allowing full use of the nuclear magnetization available, compared with the much lower flip angles used in 3D spoiled FLASH sequences ( $5^\circ$  and  $3^\circ$  used in the first and second volume, respectively, in our MP2RAGE implementation). Prior to implementation of the study we optimized the RF pulses to optimize slice profile whilst minimizing side-bands, as imperfect thin slice profiles can leave some signal un-acquired in multi-slice 2D imaging. For the NIST spherical phantom, we measured higher SNR per unit time for  $T_1$  maps generated with MS-IR-EPI than with MP2RAGE. Use of a shorter TR improves the SNR per unit time, at the cost of accurate  $T_1$  estimation. When SMS acquisition was used, SNR was found to decrease only marginally.

In brain imaging, the SNR per unit time in GM was higher for MS-IR-EPI than in MP2RAGE  $T_1$  maps, without SMS acquisition, both with and without fat suppression, but with an SMS factor of two slices, and with fat suppression, it was slightly lower than that of MP2RAGE. Note that head motion between scans can result in errors in the estimation of the noise, measured as the difference between the two scans. In SMS acquisitions, SNR is degraded by the g-factor reconstruction noise, which varies considerable between scanners and vendors. In addition to the g-factor noise penalty, non-perfectly square slice profiles can cause signal loss within a slice due to partial saturation resulting from RF excitation meant for an adjacent slice. Ideal slice profiles are harder to achieve for thinner slices, particularly when using SMS excitation. Another noise contribution is introduced by the fitting procedure required for the  $T_1$  mapping in MS-IR-EPI, compared with MP2RAGE which uses a look-up table. To reduce this source of noise, a look-up table could also be used to estimate  $T_1$  in MS-IR-EPI, as previous studies have shown (Renvall et al., 2016; Cohen and Polimeni, 2018).

Comparisons here were performed for a whole brain volume, where the SNR for 3D volumetric sequences such as MP2RAGE is optimal. By contrast, in applications for which only a partial brain volume is required, multi-slice sequences such as MS-IR-EPI incur no loss of SNR, and hence can provide better SNR per unit time.

Here, we have compared MP2RAGE and MS-IR-EPI acquisitions accelerated by parallel imaging techniques. However, recent advances in image reconstruction based on deep learning algorithms can be used to highly accelerate the acquisition in MP2RAGE (Lønning et al., 2019) and multi-shot EPI (Bilgic et al., 2019). Compressed sensing

(Lustig et al., 2007) has also been applied to accelerate MP2RAGE acquisitions (Trotier et al., 2019; Mussard et al., 2020).

#### 4.4. High resolution $T_1$ mapping using MS-IR-EPI and MP2RAGE

A key objective was to provide a sequence for  $T_1$  mapping which provides high SNR per unit time and sharp images to improve visualization of intra-cortical structures.  $T_1$  maps of the whole brain generated with MS-IR-EPI at the higher 0.5 mm isotropic resolution show good SNR and an exquisite level of detail. The acquisition time for 0.5 mm isotropic MS-IR-EPI data was under 20 min, considerably faster than the 60 min total acquisition time (30 min per hemisphere) reported for quantitative  $T_1$  maps of comparable SNR generated with 0.5 mm isotropic resolution using MP2RAGE at 7 T (Dinse et al., 2015). It should be highlighted that for SMS slice thicknesses of 0.5 mm, the pulse duration increases considerably to 9.7 ms, but SAR does not change with SMS factor or slice thickness (0.7 and 0.5 mm).

It has been suggested that a high spatial resolution, ideally to 0.3 mm, will be required to reliably distinguish the cortical areas solely based on intra-cortical features (Dinse et al., 2015). For this purpose, it is crucial that the nominal spatial resolution is not compromised by a poor PSF. But a slice profile for an ultra-thin slice (0.3 mm), is more difficult to achieve in 2D (as compared to 3D), due to the longer RF pulses to achieve a nominally rectangular slice profile and small side lobes to minimize slice-to-slice crosstalk. Here, we compared  $T_1$  maps generated from data acquired from the occipital pole of a volunteer subject with  $0.35 \times 0.35 \times 0.7$  mm<sup>3</sup> resolution using MS-IR-EPI and MP2RAGE, taking a plane of section generally perpendicular to the calcarine sulcus. Although higher resolution is required to resolve the stria of Gennari in areas of high curvature, the cortical profiles across the striate cortex (calcarine sulcus) and extra-striate cortex from  $T_1$  maps generated using MS-IR-EPI are distinct, showing a clear dip in  $T_1$  indicating the presence of the Stria of Gennari, whereas this is not clearly evident for the  $T_1$  map generated using MP2RAGE (Fig. 8B). This finding is consistent with a narrower point spread function for the MS-IR-EPI acquisition compared to the MP2RAGE acquisition. In MP2RAGE the signal recovery during the acquisition window (1276.7 ms), which is relatively long with respect to  $T_1$  of GM and WM tissue, induces  $T_1$  blurring in the resulting image, which can be exacerbated by incorrectly chosen flip angles. In MS-IR-EPI there is less  $T_1$  relaxation during the short readout ( $BW=41$  Hz/duration=24.4 ms) and hence less  $T_1$ -induced blurring.

MS-IR-EPI images can also be prone to blurring in the phase encoding direction, associated with the relatively short  $T_2^*$ , due to the lines of k-space being acquired at different times. In our implementation this effect is minimal due to the short acquisition window used, resulting from a high readout bandwidth and low EPI factor (see Table 1), though the acquisition window may be significant relative to the  $T_2^*$  of tissue in areas of high susceptibility (due to iron, air, etc.). It is also worth noting that the use of motion correction across the individual MS-IR-EPI volumes may have introduced additional image blurring (uncorrected subject motion also introduces image blurring); however, even with these additional sources of blurring, the effective resolution of MS-IR-EPI was superior to that of MP2RAGE. The improved sharpness of MS-IR-EPI and efficiency (faster than MP2RAGE) highlight the feasibility of MS-IR-EPI for improving the spatial resolution of  $T_1$  mapping for the purpose of in-vivo cortical parcellation using myeloarchitecture.

For fully quantitative  $T_1$  analysis, a long TR (at least 5 s) is required. However, for the purpose of cortical parcellation, where the relative  $T_1$  profile across the cortex is of greatest interest, a shorter TR could be used to speed up the acquisition. Note, however, that a longer TR can be used to improve SNR, in place of signal averaging. For the purpose of cortical parcellation MS-IR-EPI presents an additional advantage as it also provides a  $S_0$  parameter fit, which is a map of proton density (with a small amount of  $T_2^*$  weighting), thus providing an additional contrast that could be used in conjunction with the  $T_1$  map to assist in cortical parcellation.

Although the aim of this study was to collect very high resolution  $T_1$  maps with excellent spatial fidelity, it should be noted that this MS-IR-EPI scheme can be adapted to acquire  $T_1$  maps which are distortion-matched to fMRI data acquisitions, by adjusting the acquisition bandwidth. This can provide 0.3 mm isotropic resolution  $T_1$  structural maps useful in cortical depth-dependant fMRI applications in fMRI space, especially important given the role of such maps in intra-cortical parcellation.

#### 4.5. Considerations for ultra-high resolution $T_1$ mapping

In order to obtain  $T_1$  maps with such spatial resolution as high as 0.3 mm isotropic, prospective motion correction methods, using either an optical tracking system (Zaitsev et al., 2006), NMR field probes (De Zanche et al., 2008), fat navigators (Versluis et al., 2010) or a combination of those, are highly desirable to overcome the increased sensitivity to very small movements likely to occur during the extended acquisition times. NMR field probes are sensitive to respiration in high magnetic fields (Boer et al., 2012; Vannesjo et al., 2015) and hence can correct artefacts due to both true motion and breathing. Since multi-shot EPI acquisitions are sensitive to dynamic  $B_0$ -field fluctuations between shots, correction methods using NMR field probes can potentially improve the quality of multi-shot EPI data. A recent method has been proposed to improve image quality and quantitative metrics in multi-shot  $T_2^*$ -weighted imaging by retrospectively correcting for respiration induced  $B_0$ -fluctuations with a respiratory trace (Vannesjo et al., 2019).

The slice profile of the slice-selective excitation pulses is another factor that requires attention when reducing the slice thickness for ultra-high spatial resolution imaging. Ideal rectangular profiles are harder to achieve for thin slices, which require long RF pulse durations, particularly when combined with SMS acquisitions. The use of high slice acceleration factors in SMS acquisitions can lead to RF pulses with high peak voltage and hence increased SAR. Several methods have been proposed to reduce SAR, for example by combining SMS pulses with parallel transmission, which also provides a more uniform excitation (Wu et al., 2013; Poser et al., 2014). Another way to reduce the maximum  $B_1$  amplitude is to increase the pulse length; for the SMS acquisitions described in this paper, the maximum  $B_1$  amplitude was limited to 5 mT, resulting in a modest increase in SAR (4%) for MS1/MS2 sequences, but larger (22%) for the 0.5 mm isotropic acquisition (MS3, SMS=3) with respect to the single slice excitation acquisition. The RF pulse duration (9.6 ms) required for 0.5 mm thick slices is significant longer than the pulse duration for a single slice acquisition (3.6 ms), leading to increase TE (14 instead of 12 ms) and making sharp slice profiles harder to achieve. In order to minimize interference from neighbouring slices due to non-perfectly square slice profiles, interleaved slice excitation schemes, which can be implemented with SMS imaging (Setsompop et al., 2012), can be employed. Alternatively, methods that acquire the image volume twice (with a spatial shift in the slice direction between acquisitions) and combine the data using an iterative super-resolution algorithm (Greenspan et al., 2002) can be explored to increase the resolution in the slice select direction with improved edge definition.

## 5. Conclusion

Accurate  $T_1$  quantification is feasible using our proposed novel image processing method, which corrects for the nontrivial magnetization transfer effects on  $T_1$  caused by the necessary spectrally-selective fat-suppression pulses. This implementation of MS-IR-EPI provides fast  $T_1$  maps which are sharper than those obtained with MP2RAGE. These methods could be applied to study quantitative measures of myelin in normally appearing white matter in clinical populations compared to the healthy brain (e.g. in multiple sclerosis (Al-Radaideh et al., 2015) and neuromyelitis optica (Chou et al., 2019)) to study intracortical demyelination processes in clinical conditions (e.g. in Alzheimer's disease

(Luo et al., 2019) or multiple sclerosis (Mougín et al., 2016; Beck et al., 2018)), and to improve discrimination of functionally relevant cortical areas in human brain to correlate with fMRI studies.

## Declaration of Competing Interest

None.

## Credit authorship contribution statement

**Rosa M. Sanchez Panchuelo:** Data curation, Formal analysis, Methodology, Conceptualization, Funding acquisition, Writing – original draft. **Olivier Mougín:** Data curation, Formal analysis, Methodology, Conceptualization, Writing – review & editing. **Robert Turner:** Methodology, Conceptualization, Writing – review & editing. **Susan T. Francis:** Methodology, Conceptualization, Funding acquisition, Writing – review & editing.

## Acknowledgements

This work was funded by a Leverhulme Trust fellowship to RSP and supported by the UK Medical Research Council [grant number MR/M022722/1].

## Data and code availability statement

Python code to generate  $T_1$  maps and example dataset are available via GitHub (<https://github.com/oliviermougin/T1-mapping-IR-MS-EPI>).

We are willing and able to provide raw and/or pre-processed data on request.

## Supplementary materials

Supplementary material associated with this article can be found, in the online version, at doi:10.1016/j.neuroimage.2021.117976.

## References

- Al-Radaideh, A., Mougín, O.E., Lim, S.-Y., Chou, I.-J., Constantinescu, C.S., Gowland, P., 2015. Histogram analysis of quantitative T1 and MT maps from ultrahigh field MRI in clinically isolated syndrome and relapsing-remitting multiple sclerosis. *NMR Biomed.* 28, 1374–1382. doi:10.1002/nbm.3385.
- Bazin, P.-L., Alkemade, A., van der Zwaag, W., Caan, M., Mulder, M., Forstmann, B.U., 2019. Denoising high-field multi-dimensional MRI with local complex PCA. *Front. Neurosci.* 13, 1066. doi:10.3389/fnins.2019.01066.
- Beck, E.S., Sati, P., Sethi, V., Kober, T., Dewey, B., Bhargava, P., et al., 2018. Improved visualization of cortical lesions in multiple sclerosis using 7T MP2RAGE. *Am. J. Neuroradiol.* 39, 459–466. doi:10.3174/ajnr.A5534.
- Bilgic, B., Chatnuntawech, I., Manhard, M.K., Tian, Q., Liao, C., Iyer, S.S., et al., 2019. Highly accelerated multishot echo planar imaging through synergistic machine learning and joint reconstruction. *Magn. Reson. Med.* 82, 1343–1358. doi:10.1002/mrm.27813.
- Boer, V.O., Vd Bank, B.L., Van Vliet, G., Luijten, P.R., Klomp, D.W.J., 2012. Direct B0 field monitoring and real-time B0 field updating in the human breast at 7 tesla. *Magn. Reson. Med.* 67, 586–591. doi:10.1002/mrm.23272.
- Caan, M.W.A., Bazin, P.L., Marques, J.P., de Hollander, G., Dumoulin, S.O., van der Zwaag, W., 2019. MP2RAGEME: t1, T2\*, and QSM mapping in one sequence at 7 tesla. *Hum. Brain Mapp.* 40, 1786–1798. doi:10.1002/hbm.24490.
- Callaghan, M.F., Helms, G., Lutti, A., Mohammadi, S., Weiskopf, N., 2015. A general linear relaxometry model of  $R_1$  using imaging data. *Magn. Reson. Med.* 73, 1309–1314. doi:10.1002/mrm.25210.
- Castets, C.R., Ribot, E.J., Lefrançois, W., Trotier, A.J., Thiaudière, E., Franconi, J.-M., et al., 2015. Fast and robust 3D  $T_1$  mapping using spiral encoding and steady RF excitation at 7T: application to cardiac manganese enhanced MRI (MEMRI) in mice. *NMR Biomed.* 28, 881–889. doi:10.1002/nbm.3327.
- Cheng, H.-L.M., Stikov, N., Ghugre, N.R., Wright, G.A., 2012. Practical medical applications of quantitative MR relaxometry. *J. Magn. Reson. Imaging* 36, 805–824. doi:10.1002/jmri.23718.
- Chou, I.J., Tanasescu, R., Mougín, O.E., Gowland, P.A., Tench, C.R., Whitehouse, W.P., et al., 2019. Reduced myelin signal in normal-appearing white matter in neuromyelitis optica measured by 7T magnetic resonance imaging. *Sci. Rep.* 9. doi:10.1038/s41598-019-50928-0.
- Clare, S., Jezzard, P., 2001. Rapid T1 mapping using multislice echo planar imaging. *Magn. Reson. Med.* 45, 630–634. doi:10.1002/mrm.1085.

- Cohen, O., Polimeni, J.R., 2018. Optimized inversion-time schedules for quantitative T1 measurements based on high-resolution multi-inversion EPI. *Magn. Reson. Med.* 79, 2101–2112. doi:10.1002/mrm.26889.
- De Zanche, N., Barmet, C., Nordmeyer-Massner, J., Pruessmann, K.P., 2008. NMR probes for measuring magnetic fields and field dynamics in MR systems. *Magn. Reson. Med.* 60, 176–186. doi:10.1002/mrm.21624.
- Deichmann, R., Hahn, D., Haase, A., 1999. Fast T1 mapping on a whole-body scanner. *Magn. Reson. Med.* 42, 206–209. doi:10.1002/(sici)1522-2594(199907)42:1<206::aid-mrm28>3.0.co;2-q.
- Dieringer, M.A., Deimling, M., Santoro, D., Wuerfel, J., Madai, V.I., Sobesky, J., et al., 2014. Rapid parametric mapping of the longitudinal relaxation time T1 using two-dimensional variable flip angle magnetic resonance imaging at 1.5 Tesla, 3 Tesla, and 7 Tesla. *PLoS ONE* 9. doi:10.1371/journal.pone.0091318.
- Dinse, J., Härtlich, N., Waehnert, M.D., Tardif, C.L., Schäfer, A., Geyer, S., et al., 2015. A cytoarchitecture-driven myelin model reveals area-specific signatures in human primary and secondary areas using ultra-high resolution in-vivo brain MRI. *Neuroimage* 114, 71–87. doi:10.1016/j.neuroimage.2015.04.023.
- Dougherty, R., Mezer, A., Zhu, K., Kerr, A., Middione, A., 2014. Fast quantitative T1 mapping with simultaneous multi-slice EPI. *Org. Hum. Brain. Map.* 2002.
- Eminian, S., Hajdu, S.D., Meuli, R.A., Maeder, P., Hagmann, P., 2018. Rapid high resolution T1 mapping as a marker of brain development: normative ranges in key regions of interest. *PLoS ONE* 13. doi:10.1371/journal.pone.0198250.
- Federau, C., Gallichan, D., 2016. Motion-correction enabled ultra-high resolution in-vivo 7T-MRI of the brain. *PLoS ONE* 11, e0154974. doi:10.1371/journal.pone.0154974.
- Geyer, S., Weiss, M., Reimann, K., Lohmann, G., Turner, R., 2011. Microstructural parcellation of the human cerebral cortex – from Brodmann’s post-mortem map to in vivo mapping with high-field magnetic resonance imaging. *Front. Hum. Neurosci.* 5. doi:10.3389/fnhum.2011.00019.
- Glasser, M.F., Coalson, T.S., Robinson, E.C., Hacker, C.D., Harwell, J., Yacoub, E., et al., 2016. A multi-modal parcellation of human cerebral cortex. *Nature* 536, 171–178. doi:10.1038/nature18933.
- Glasser, M.F., van Essen, D.C., 2011. Mapping human cortical areas in vivo based on myelin content as revealed by T1- and T2-weighted MRI. *J. Neurosci.* 31, 11597–11616. doi:10.1523/JNEUROSCI.2180-11.2011.
- Gochberg, D.F., Gore, J.C., 2007. Quantitative magnetization transfer imaging via selective inversion recovery with short repetition times. *Magn. Reson. Med.* 57, 437–441. doi:10.1002/mrm.21143.
- Gowland, P., Mansfield, P., 1993. Accurate measurement of T1 in vivo in less than 3 s using echo-planar imaging. *Magn. Reson. Med.* 30, 351–354. doi:10.1002/mrm.1910030032.
- Greenspan, H., Oz, G., Kiryati, N., Pelez, S., 2002. MRI inter-slice reconstruction using super-resolution. *Magn. Reson. Imaging* 20, 437–446.
- Gristeadt, J.W., Wang, D., Bhat, H., 2014. Slice-accelerated inversion recovery T1 mapping. *Int. Soc. Mag. Res. Med.* 2318.
- Haast, R.A.M., Ivanov, D., Uludağ, K., 2018. The impact of B1+ correction on MP2RAGE cortical T1 and apparent cortical thickness at 7T. *Hum. Brain Mapp* 39, 2412–2425. doi:10.1002/hbm.24011.
- Hagiwara, A., Hori, M., Cohen-Adad, J., Nakazawa, M., Suzuki, Y., Kasahara, A., et al., 2019. Linearity, bias, intrascanner repeatability, and interscanner reproducibility of quantitative multidynamic multiecho sequence for rapid simultaneous relaxometry at 3 T. *Invest. Radiol.* 54, 39–47. doi:10.1097/RLI.0000000000000510.
- Huber, L., Marrett, S., Handwerker, D.A., Thomas, A., Gutierrez, B., Steel, C., et al., 2016. Fast dynamic measurement of functional T1 and grey matter thickness changes during brain activation at 7T. *In Proc. Int. Soc. Magn. Reson. Med.* 2209.
- Hurley, A.C., Al-Radaideh, A., Bai, L., Aickelin, U., Coxon, R., Glover, P., et al., 2010. Tailored RF pulse for magnetization inversion at ultrahigh field. *Magn. Reson. Med.* 63, 51–58. doi:10.1002/mrm.22167.
- Kashyap, S., Ivanov, D., Havlicek, M., Poser, B.A., Uludağ, K., 2018. Impact of acquisition and analysis strategies on cortical depth-dependent fMRI. *Neuroimage* 168, 332–344. doi:10.1016/j.neuroimage.2017.05.022.
- Kato, Y., Ichikawa, K., Okudaira, K., Taoka, T., Kawaguchi, H., Murata, K., et al., 2019. Comprehensive evaluation of B1+-corrected FISP-based magnetic resonance fingerprinting: accuracy, repeatability and reproducibility of T1 and T2 relaxation times for ISMRM/NIST system phantom and volunteers. *Magn. Reson. Med. Sci.* doi:10.2463/mrms.mp.2019-0016.
- Kenan, K., Stupic, K.F., Boss, M.A., Russek, S.E., Chenevert, T.L., Prasad, P.V., et al., 2016. Comparison of T1 measurement using ISMRM/NIST system phantom | NIST. *In: Proc. Int. Soc. Magn. Reson. Med.*, p. 3290.
- Koenig, S.H., Brown, R.D., Spiller, M., Lundbom, N., 1990. Relaxometry of brain: why white matter appears bright in MRI. *Magn. Reson. Med.* 14, 482–495. doi:10.1002/mrm.1910140306.
- Kucharczyk, W., Macdonald, P.M., Stanisz, G.J., Henkelman, R.M., 1994. Relaxivity and magnetization transfer of white matter lipids at MR imaging: importance of cerebrospines and pH. *Radiology* 192, 521–529. doi:10.1148/radiology.192.2.8029426.
- Kupeli, A., Kocak, M., Goktepel, M., Karavas, E., Danisan, G., 2020. Role of T1 mapping to evaluate brain aging in a healthy population. *Clin. Imaging* 59, 56–60. doi:10.1016/j.clinimag.2019.09.005.
- Labadie, C., Lee, J.-H., Rooney, W.D., Jarchow, S., Aubert-Frécon, M., Springer, C.S., et al., 2014. Myelin water mapping by spatially regularized longitudinal relaxographic imaging at high magnetic fields. *Magn. Reson. Med.* 71, 375–387. doi:10.1002/mrm.24670.
- Laun, M.L., McCreary, C.R., Frayne, R., 2016. Multislice T1-prepared 2D single-shot EPI: analysis of a clinical T1 mapping method unbiased by B0 or B1 inhomogeneity. *NMR Biomed.* 29, 1056–1069. doi:10.1002/nbm.3566.
- Leuze, C., Aswendt, M., Ferenczi, E., Liu, C.W., Hsueh, B., Goubran, M., et al., 2017. The separate effects of lipids and proteins on brain MRI contrast revealed through tissue clearing. *Neuroimage* 156, 412–422. doi:10.1016/j.neuroimage.2017.04.021.
- Li, K., Zu, Z., Xu, J., Janve, V.A., Gore, J.C., Does, M.D., et al., 2010. Optimized inversion recovery sequences for quantitative T1and magnetization transfer imaging. *Magn. Reson. Med.* 64, 491–500. doi:10.1002/mrm.22440.
- Lønning, K., Putzky, P., Sonke, J.J., Reneman, L., Caan, M.W.A., Welling, M., 2019. Recurrent inference machines for reconstructing heterogeneous MRI data. *Med. Image Anal.* 53, 64–78. doi:10.1016/j.media.2019.01.005.
- Look, D.C., Locker, D.R., 1970. Time saving in measurement of NMR and EPR relaxation times. *Rev. Sci. Instrum.* 41, 250–251. doi:10.1063/1.1684482.
- Luo, X., Li, K., Zeng, Q., Huang, P., Jiaerken, Y., Wang, S., et al., 2019. Application of T1-/T2-weighted ratio mapping to elucidate intracortical demyelination process in the Alzheimer’s disease continuum. *Front. Neurosci.* 13, 904. doi:10.3389/fnins.2019.00904.
- Lustig, M., Donoho, D., Pauly, J.M., 2007. Sparse MRI: the application of compressed sensing for rapid MR imaging. *Magn. Reson. Med.* 58, 1182–1195. doi:10.1002/mrm.21391.
- Lutti, A., Dick, F., Sereno, M.I., Weiskopf, N., 2014. Using high-resolution quantitative mapping of R1 as an index of cortical myelination. *Neuroimage* 93 (Pt 2), 176–188. doi:10.1016/j.neuroimage.2013.06.005.
- Marques, J.P., Gruetter, R., 2013. New developments and applications of the MP2RAGE sequence - focusing the contrast and high spatial resolution R1 mapping. *PLoS ONE* 8. doi:10.1371/journal.pone.0069294.
- Marques, J.P., Kober, T., Krueger, G., van der Zwaag, W., Van de Moortele, P.F., Gruetter, R., 2010. MP2RAGE, a self bias-field corrected sequence for improved segmentation and T1-mapping at high field. *Neuroimage* 49, 1271–1281. doi:10.1016/j.neuroimage.2009.10.002.
- Meterer, R., Kober, T., Möller, H.E., Schäfer, A., 2017. Simultaneous quantitative MRI mapping of T1, T2\* and magnetic susceptibility with multi-echo MP2RAGE. *PLoS ONE* 12, e0169265.
- Mougín, O., Abdel-Fahim, R., Dineen, R., Pitiot, A., Evangelou, N., Gowland, P., 2016. Imaging gray matter with concomitant null point imaging from the phase sensitive inversion recovery sequence. *Magn. Reson. Med.* 76, 1512–1516. doi:10.1002/mrm.26061.
- Mougín, O., Clemence, M., Peters, A., Pitiot, A., Gowland, P., 2013. High-resolution imaging of magnetisation transfer and nuclear overhauser effect in the human visual cortex at 7 T. *NMR Biomed* 26, 1508–1517. doi:10.1002/nbm.2984.
- Mussard, E., Hilbert, T., Forman, C., Meuli, R., Thiran, J., Kober, T., 2020. Accelerated MP2RAGE imaging using Cartesian phyllotaxis readout and compressed sensing reconstruction. *Magn. Reson. Med.* 84, 1881–1894. doi:10.1002/mrm.28244.
- Nofeie, J.T., Cheng, H.L.M., 2013. Ultrashort echo time for improved positive-contrast manganese-enhanced MRI of cancer. *PLoS ONE* 8. doi:10.1371/journal.pone.0058617.
- Ordidge, R.J., Gibbs, P., Chapman, B., Stehling, M.K., Mansfield, P., 1990. High-speed multislice T1 mapping using inversion-recovery echo-planar imaging. *Magn. Reson. Med.* 16, 238–245. doi:10.1002/mrm.1910160205.
- Polders, D.L., Leemans, A., Luijten, P.R., Hoogduin, H., 2012. Uncertainty estimations for quantitative in vivo MRI T1 mapping. *J. Magn. Reson.* 224, 53–60. doi:10.1016/j.jmr.2012.08.017.
- Poser, B.A., Anderson, R.J., Guérin, B., Setsompop, K., Deng, W., Mareyam, A., et al., 2014. Simultaneous multislice excitation by parallel transmission. *Magn. Reson. Med.* 71, 1416–1427. doi:10.1002/mrm.24791.
- Prantner, A.M., Bretthorst, G.L., Neil, J.J., Garbow, J.R., Ackerman, J.J.H., 2008. Magnetization transfer induced biexponential longitudinal relaxation. *Magn. Reson. Med.* 60, 555–563. doi:10.1002/mrm.21671.
- Renvall, V., Witzel, T., Wald, L.L., Polimeni, J.R., 2016. Automatic cortical surface reconstruction of high-resolution T1 echo planar imaging data. *Neuroimage* 134, 338–354. doi:10.1016/j.neuroimage.2016.04.004.
- Rioux, J.A., Levesque, I.R., Rutt, B.K., 2016. Biexponential longitudinal relaxation in white matter: characterization and impact on T1 mapping with IR-FSE and MP2RAGE. *Magn. Reson. Med.* 75, 2265–2277. doi:10.1002/mrm.25729.
- Rooney, W.D., Johnson, G., Li, X., Cohen, E.R., Kim, S.G., Ugurbil, K., et al., 2007. Magnetic field and tissue dependencies of human brain longitudinal 1H2O relaxation in vivo. *Magn. Reson. Med.* 57, 308–318. doi:10.1002/mrm.21122.
- Rui, R.P., Neji, R., Wood, T.C., Baburamani, A.A., Malik, S.J., Hajnal, J.V., 2020. Controlled saturation magnetization transfer for reproducible multivendor variable flip angle T1 and T2 mapping. *Magn. Reson. Med.* 84, 221–236. doi:10.1002/mrm.28109.
- Sánchez-Panchuelo, R.M., Francis, S.T., Schluppeck, D., Bowtell, R.W., 2012. Correspondence of human visual areas identified using functional and anatomical MRI in vivo at 7 T. *J. Magn. Reson. Imaging* 35, 287–299. doi:10.1002/jmri.22822.
- Sanchez Panchuelo, R.M., Turner, R., Mougín, O.E., Francis, S.T., 2018. A 2D multi-shot IR EPI T1 mapping. *In Proc. Intl. Soc. Mag. Reson. Med.* 26.
- Santyr, G.E., 1993. Magnetization transfer effects in multislice MR imaging. *Magn. Reson. Imaging* 11, 521–532. doi:10.1016/0730-725x(93)90471-o.
- Sereno, M., Lutti, A., Weiskopf, N., Dick, F., 2013. Mapping the human cortical surface by combining quantitative T1 with retinotopy. *Cereb. Cortex* 23, 2261–2268. doi:10.1093/cercor/bhs213.
- Setsompop, K., Cohen-Adad, J., Gagoski, B.A., Raij, T., Yendiki, A., Keil, B., et al., 2012. Improving diffusion MRI using simultaneous multi-slice echo planar imaging. *Neuroimage* 63, 569–580. doi:10.1016/j.neuroimage.2012.06.033.
- Shin, W., Gu, H., Yang, Y., 2009. Incidental magnetization transfer contrast by fat saturation preparation pulses in multislice look-locker echo planar imaging. *Magn. Reson. Med.* 62, 520–526. doi:10.1002/mrm.22034.

- Stikov, N., Boudreau, M., Levesque, I.R., Tardif, C.L., Barral, J.K., Pike, G.B., 2015. On the accuracy of T1 mapping: searching for common ground. *Magn. Reson. Med.* 73, 514–522. doi:10.1002/mrm.25135.
- Stüber, C., Morawski, M., Schäfer, A., Labadie, C., Wähnert, M., Leuze, C., et al., 2014. Myelin and iron concentration in the human brain: a quantitative study of MRI contrast. *Neuroimage* 93 (Pt 1), 95–106. doi:10.1016/j.neuroimage.2014.02.026.
- Thangavel, K., Ulkü, E., Saritas, I., S., 2017. Aqueous paramagnetic solutions for MRI phantoms at 3 T: a detailed study on relaxivities. *Turkish J. Electr. Eng. Comput. Sci.* 25, 2108–2121. doi:10.3906/elk-1602-123.
- Trampel, R., Bazin, P.L., Pine, K., Weiskopf, N., 2019. In-vivo magnetic resonance imaging (MRI) of laminae in the human cortex. *Neuroimage* 197, 707–715. doi:10.1016/j.neuroimage.2017.09.037.
- Trotier, A.J., Rapacchi, S., Faller, T.L., Miraux, S., Ribot, E.J., 2019. Compressed-Sensing MP2RAGE sequence: application to the detection of brain metastases in mice at 7T. *Magn. Reson. Med.* 81, 551–559. doi:10.1002/mrm.27438.
- Turner, R., 2019. Myelin and modeling: bootstrapping cortical microcircuits. *Front. Neural Circuits* 13. doi:10.3389/fncir.2019.00034.
- Turner, R., Geyer, S., 2014. Comparing like with like: the power of knowing where you are. *Brain Connect.* 4, 547–557. doi:10.1089/brain.2014.0261.
- Turner, R., Oros-Peusquens, A.M., Romanzetti, S., Zilles, K., Shah, N.J., 2008. Optimised in vivo visualisation of cortical structures in the human brain at 3 T using IR-TSE. *Magn. Reson. Imaging* 26, 935–942. doi:10.1016/j.mri.2008.01.043.
- Van de Moortele, P.F., Auerbach, E.J., Olman, C., Yacoub, E., Uğurbil, K., Moeller, S., 2009. T1 weighted brain images at 7 Tesla unbiased for Proton Density, T2\* contrast and RF coil receive B1 sensitivity with simultaneous vessel visualization. *Neuroimage* 46, 432–446. doi:10.1016/j.neuroimage.2009.02.009.
- Vannesjo, S.J., Clare, S., Kasper, L., Tracey, I., Miller, K.L., 2019. A method for correcting breathing-induced field fluctuations in T2\*-weighted spinal cord imaging using a respiratory trace. *Magn. Reson. Med.* 81, 3745–3753. doi:10.1002/mrm.27664.
- Vannesjo, S.J., Wilm, B.J., Duerst, Y., Gross, S., Brunner, D.O., Dietrich, B.E., et al., 2015. Retrospective correction of physiological field fluctuations in high-field brain MRI using concurrent field monitoring. *Magn. Reson. Med.* 73, 1833–1843. doi:10.1002/mrm.25303.
- Versluis, M.J., Peeters, J.M., van Rooden, S., van der Grond, J., van Buchem, M.A., Webb, A.G., et al., 2010. Origin and reduction of motion and f0 artifacts in high resolution T2\*-weighted magnetic resonance imaging: application in Alzheimer's disease patients. *Neuroimage* 51, 1082–1088. doi:10.1016/j.neuroimage.2010.03.048.
- Waehnert, M.D., Dinse, J., Weiss, M., Streicher, M.N., Waehnert, P., Geyer, S., et al., 2014. Anatomically motivated modeling of cortical laminae. *Neuroimage* 93, 210–220. doi:10.1016/j.neuroimage.2013.03.078.
- Waehnert, M.D., Dinse, J., Schäfer, A., Geyer, S., Bazin, P.L., Turner, R., Tardif, C.L., 2016. A subject-specific framework for in vivo myeloarchitectonic analysis using high resolution quantitative MRI. *Neuroimage* 125, 94–107. doi:10.1016/j.neuroimage.2015.10.001.
- Weiss, G.H., Gupta, R.K., Ferretti, J.A., Becker, E.D., 1980. The choice of optimal parameters for measurement of spin-lattice relaxation times. I. Mathematical formulation. *J. Magn. Reson.* 37, 369–379. doi:10.1016/0022-2364(80)90044-X.
- Wright, P.J., Mougín, O.E., Totman, J.J., Peters, A.M., Brookes, M.J., Coxon, R., et al., 2008. Water proton T1 measurements in brain tissue at 7, 3, and 1.5T using IR-EPI, IR-TSE, and MPRAGE: results and optimization. *Magn. Reson. Mater. Physics, Biol. Med.* 21, 121–130. doi:10.1007/s10334-008-0104-8.
- Wu, X., Schmitter, S., Auerbach, E.J., Moeller, S., Uğurbil, K., Van De Moortele, P.F., 2013. Simultaneous multislice multiband parallel radiofrequency excitation with independent slice-specific transmit B1 homogenization. *Magn. Reson. Med.* 70, 630–638. doi:10.1002/mrm.24828.
- Yarnykh, V.L., 2007. Actual flip-angle imaging in the pulsed steady state: a method for rapid three-dimensional mapping of the transmitted radiofrequency field. *Magn. Reson. Med.* 57, 192–200. doi:10.1002/mrm.21120.
- Yen, Y., Keenan, K., Stupic, K., van der Kouwe, A., Polimeni, J., 2017. T1 mapping of the NIST phantom at 7T. In: *Proc. Int. Soc. Magn. Reson. Med.*, p. 5207.
- Zaitsev, M., Dold, C., Saka, G., Hening, J., Speck, O., 2006. Magnetic resonance imaging of freely moving objects: prospective real-time motion correction using an external optical motion tracking system. *Neuroimage* 31, 1038–1050. doi:10.1016/j.neuroimage.2006.01.039.